Energy Mapping of Scattered Protons
Within a Gas Target

by

Julia Georgina Publicover
B.Sc., Dalhousie University, 2002

A Thesis Submitted in Partial Fulfillment of the
Requirements for the Degree of

MASTER OF SCIENCE

in the Department of Physics and Astronomy

We accept this thesis as conforming
to the required standard

Supervisors: Dr. T.J. Ruth, Dr. J.M. Roney

ABSTRACT

Gas targets are the most common form of target used in the production of short-lived radioisotopes for positron emission tomography (PET). Many researchers, however, have reported a non-linear relationship between radioisotope production yield and particle beam current. This lowered yield has been attributed to several factors including the scattering of beam particles into the target body walls, radioactive species becoming trapped in the target body walls, and gas density reduction due to the deposition of heat from the incident ion beam. In this study we investigate the last factor. A 13 MeV proton beam from the TRIUMF TR13 cyclotron was used to measure the energy of scattered protons in a gas target. The average proton energy reaching the target body walls was determined by measuring the ratio of radioactivity of two simultaneously produced radioisotopes in a metal foil lining the wall of the target. The relationship between the ratio of radioactivities and proton energy was determined using a stacked foil calibration technique. These experiments were compared to theory using a Monte Carlo program (SRIM) to model the interactions of a proton beam within a gas target.

Examiners:

Table of Contents

List of Tables

List of Figures

Acknowledgments

I would like to express my sincere thanks to my supervisors, Dr. Tom Ruth at TRIUMF and Dr. Mike Roney at the University of Victoria, for their guidance and support throughout this project and during my time in both Victoria and Vancouver.

I would also like to thank my colleagues at TRIUMF, Suzy Lapi, Ken Buckley, Paul Piccioni, Wayne Sievers and the entire TRIUMF PET group, for their help with the cyclotron and targets as well as offering their knowledge on many topics and the many useful discussions we have had over the past 2 years.

This research was supported through TRIUMF Life Science, CIHR, and NSERC.

Chapter 1
Introduction

1.1 Positron Emission Tomography (PET)

Positron emission tomography (PET) is a non-invasive medical imaging technique, which makes use of positron emitting radionuclides as biological indicators. When a positron is emitted through the decay of a radionuclide it will lose energy through interactions with electrons along its path. At the end of its range each positron will annihilate with an electron and give rise to two photons, which are released simultaneously at nearly 180 degrees to one another.

By placing an appropriate array of detectors around the radioactive isotope, these coincident photons can be detected and the line of response (LOR) between them can be found. To create a line of response, the two coincidence photons must arrive in opposing detectors within a predefined time of one another, typically a few nanoseconds. If one of the coincidence photons is not detected within this time limit the event is rejected. These lines of response can then be used to mathematically back-calculate the location of the annihilating positron and hence obtain a density map of radioactivity [1]. This is illustrated in Figure 1.1. The first line of response indicates that somewhere along this line positron annihilation has taken place. Each consecutive line will then determine the specific location in space by their intersection with one another. This density map can then be used to recreate image slices.

The basis of PET is that if a positron-emitting isotope is attached to a biologically important compound (radiopharmaceutical), we can then obtain the spatial and temporal distribution of that compound within an organ or biological system [1]. Table 1.1 lists several of the most common radiopharmaceuticals, along with their production route, half-lives ($t_{1/2}$), and applications.

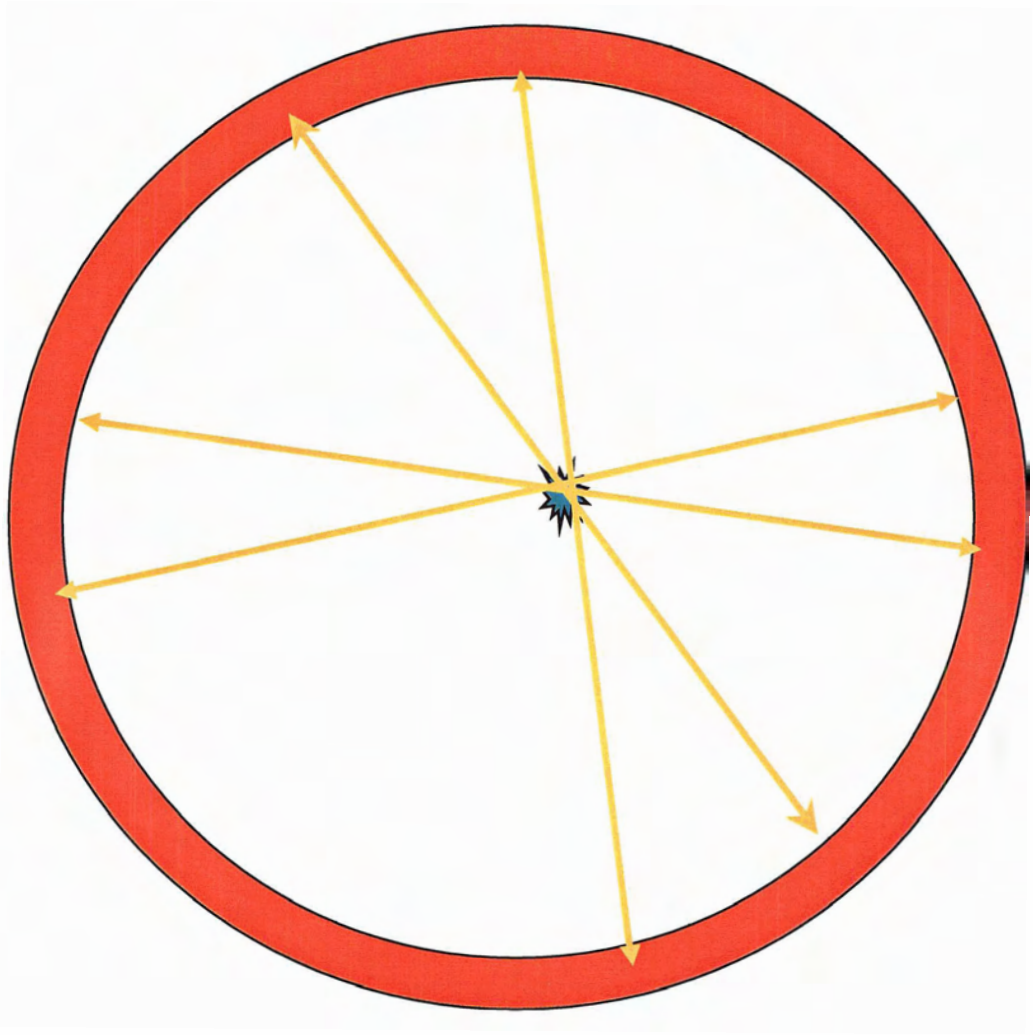

Figure 1.1: The collection of "lines of response" allows the PET computer software to back-calculate radioactivity density maps. Image courtesy of Tom Ruth.

Isotope	Nuclear Reaction	$t_{1/2}$ (minutes)	Radiopharmaceuticals	Application
^{11}C	$^{14}N(p,\alpha)^{11}C$	20.4	Raclopride	D2 receptor density
			Methylphenidate	Dopamine transporter
^{18}F	$^{18}O(p,n)^{18}F$ $^{20}Ne(d,\alpha)^{18}F$	109.8	Fluorodeoxyglucose	Glucose Utilization
			Fluorodopa	Decarboxyla-tion and storage of dopamine
^{15}O	$^{15}N(p,n)^{15}O$ $^{14}N(d,n)^{15}O$	2.03	O_2	Oxygen Metabolism
			Water	Blood Flow
			Carbon monoxide	Blood Volume
^{13}N	$^{16}O(p,\alpha)^{13}N$	9.97	Ammonia	Cardiac Blood Flow

Table 1.1: Common radiopharmaceuticals used in positron emission tomography and their applications.

The true power of PET lies in the ability to acquire quantitative functional images at extremely high sensitivity. This ability is related to the intrinsic nature of the positron decay and being able to correct for attenuation, something not easily done with SPECT (single photon emission computed tomography), and its sensitivity, on the order of picomolar concentrations, is several orders of magnitude more sensitive than MRI (magnetic resonance imaging), which achieves millimolar concentrations [1].

PET produces "functional images" [2]. With most classical diagnostic tools what is obtained is images of structures (e.g.- bones, organs, etc.); however, with PET one can image biological systems in action (e.g.- uptake of compounds). To illustrate this, consider Figure 1.2, which shows a PET image of the uptake of Fluorine-18 Fluorodopa within the striatum of the brain of a human subject with Parkinson's disease. Fluorodopa is used to measure the decarboxylation and storage of dopamine .

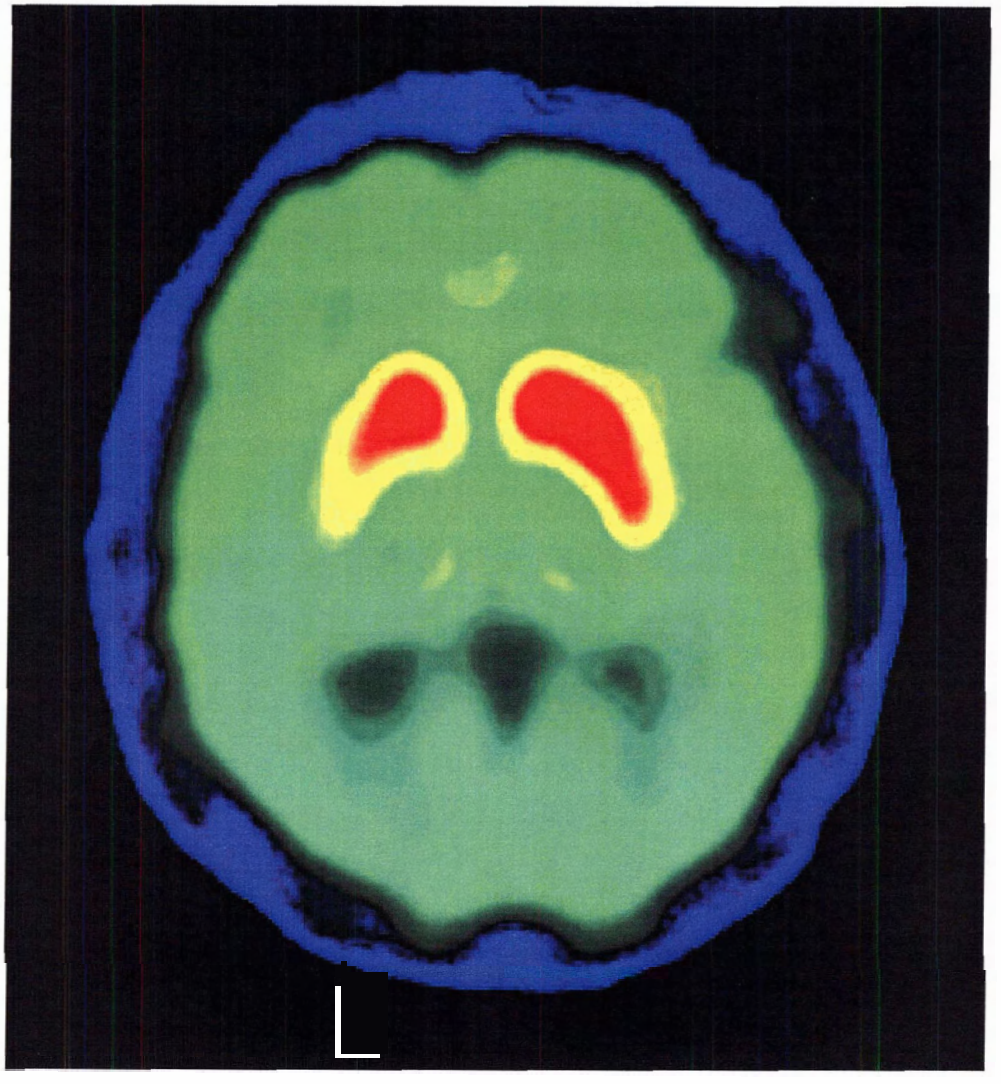

Figure 1.2: PET image of ^{18}F-fluorodopa uptake in the brain of a human subject with Parkinson's disease. The bright spots are the location of the striatum. Image courtesy of the UBC/TRIUMF PET program.

The amount of attenuation caused by the surrounding material (i.e.- the patient) can be determined by comparing the detector count rate with an external PET source (i.e.- ^{68}Ge/^{68}Ga), without any attenuating material present, to the count rate with the attenuating material present [1]. The attenuation coefficient for the two γ-rays is equal to:

$$e^{-\mu_1 x_1} \cdot e^{-\mu_2 x_2} = e^{-\mu(x_1+x_2)} \qquad \textbf{[1.1]}$$

Where x_1 and x_2 are the distances from the source to the detector and μ_1 and μ_2 are the attenuation coefficients for air and the object, respectively. This allows the reconstructed image to be corrected for attenuation [1].

Around the world PET imaging is becoming more widely available for clinical diagnostics. Recently in Canada PET centers have been established in Sherbrook QC, Ottawa ON, Edmonton AB, and Winnipeg MB in addition to the existing research facilities in Toronto, Montreal and Vancouver. The production of short-lived radiopharmaceuticals, however, is costly. While many research groups have focused on increasing radioisotope yield while minimizing the cost of production, still more information is needed to optimize this process. This thesis addresses part of this lack of information.

1.2 Radioisotope production for radiopharmaceuticals

The production of radioisotopes for nuclear medicine is generally accomplished in one of three ways: 1) by neutron reactions in a nuclear reactor, 2) by decay and separation in a generator or 3) by charged particle bombardment via a particle accelerator, usually a cyclotron. The use of cyclotrons for the production of radioisotopes for PET is by far the most common production route used today.

The TR13 cyclotron, located in the Meson Hall, at TRIUMF, Canada's National Laboratory for Nuclear and Particle Physics, in Vancouver, Canada, is a fixed energy (13 MeV), proton only, negative ion (H^-) machine. H^- ions are accelerated with the aid of radio-frequency (RF) energy and directed in a circular motion by a constant magnetic field. The RF is passed between metal plates called Dees. The proton beam is extracted by stripping both electrons off the H^- ion through a thin carbon foil. The removal of electrons not only provides the proton beam, but also changes the charge of the particle from negative to positive. Hence, the direction of motion within the magnetic field will

be reversed. This allows the protons to be directed out of the cyclotron's vacuum tank and strike the production target. The TR13 is equipped with two extraction foils allowing for the production of two simultaneous beams. A diagram of the TR13 cyclotron can be seen in Figure 1.3 and a photograph of inside the vacuum tank is found in Figure 1.4.

Radioisotopes are produced through nuclear reactions by irradiation of a material with these accelerated particles. The vessel containing the material, as well as the material to be irradiated, is referred to as the target. Target materials can be solids, liquids or gases. Solid targets, however, are rarely used in the production of PET isotopes due to the difficulty of separating the produced isotope from the target material. This process can be incredibly time consuming, which is a severe drawback when dealing with short–lived radioisotopes. Gas targets are the most commonly used form of target for PET radioisotopes. They have many advantages over the other types of targets. Including :

i. A relatively simple target chamber design because melting and boiling is not an issue.
ii. Gas transfer from the target to the laboratory is fast, clean and simple. Speed is imperative when dealing with isotopes with half-lives on the order of minutes.
iii. The separation of the radioisotope from the bulk target gas is uncomplicated. Separation is accomplished by making use of the differences in physical and/or chemical properties of the target gas and product.

Gas targets, however, suffer from density reduction in the gas due to heat being deposited by the beam of charged particles. This results in a much lower production yield as compared to the theoretical values based on available cross section data. Bida, Ruth and Wolf [3] determined that the production of Carbon-11 from the (p,α) reaction on Nitrogen gas is approximately 25% less than the yield calculated from published excitation functions and speculated that this was due to gas density reduction within the target gas . Gas density reduction is discussed in more detail in Section 2.2.

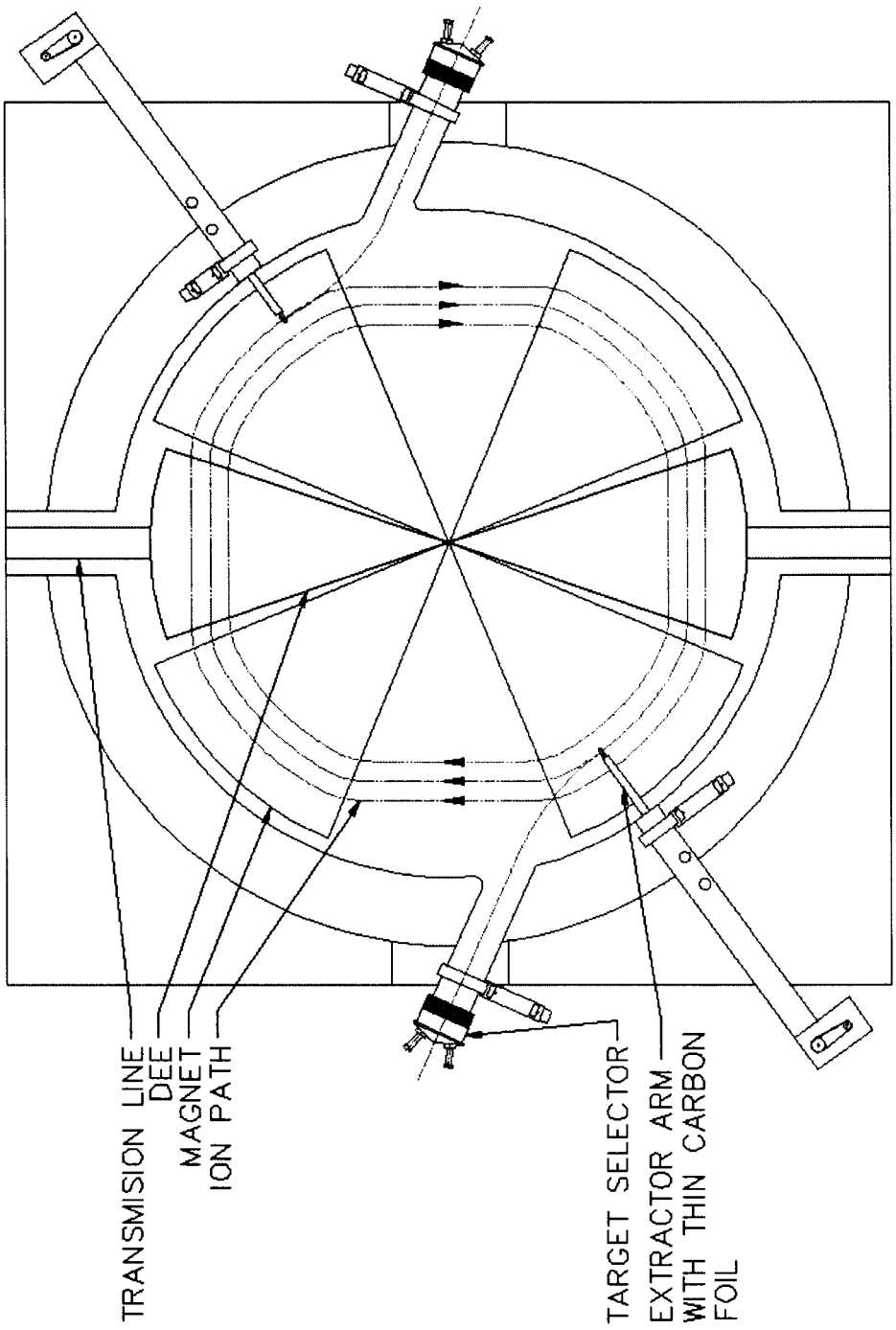

Figure 1.3: Schematic diagram of the TR13 cyclotron. The magnetic field is directed perpendicular to the plane of the cyclotron (i.e. perpendicular to the plane of the page).

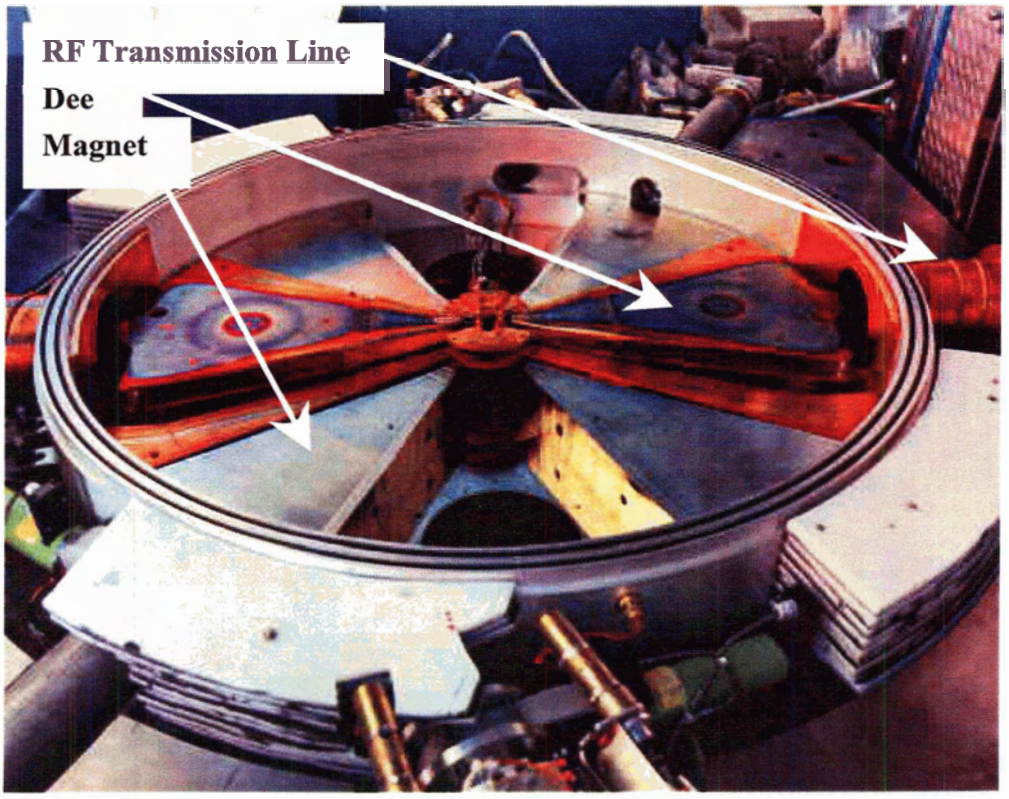

Figure 1.4: Photograph of inside the vacuum tank of the TR13 cyclotron at TRIUMF. The radio-frequency energy used to accelerate the H- ions is supplied to the Dees by the RF transmission line. The circular path of the ions is initiated by the magnetic field perpendicular to the plate.

It has also been reported that wall interactions may contribute to lower yields than predicted [4-5]. It was found that the produced radionuclide may interact with the walls of the target chamber and stick, thus reducing the recoverable yield.

Multiple coulomb scattering, as discussed in Section 2.1.2, can also reduce the production yield. The angular spread of a particle beam may become great enough that a substantial number of particles are eliminated from the production process by interacting with the target chamber walls [25-26].

Explanation and rectification of these issues with gas targets could benefit a large cross-section of fields of research. For example, within nuclear medicine alone these targets

are used to produce Iodine-123 for SPECT (Single Photon Emission Computed Tomography) [6-7], many isotopes for PET as noted above (^{11}C, ^{15}O, ^{18}F) [3, 8-11], as well as for other less common isotopes such as Rubidium-82 [12]. There has also been great interest in gas targets for nuclear physics [13-14], particularly in recent studies for radioactive ion beams used in nuclear physics and astrophysics experiments [15].

Demystifying the processes taking place within gas targets has been an active area of study for many years now with the ultimate goal of being able to irradiate a target at high beam currents and achieve near theoretical yield. To date, however, little headway has been made into quantitatively explaining these effects. The aim of this project was to increase our knowledge of the processes taking place within a gas target, and make steps towards an optimized gas target production system. Some of the questions we would like to answers with our research are: 1) Do the light emission photographs, taken by Heselius et al [16], accurately represent the beam profile? 2) Does the theoretical proton beam scatter profile, as predicted using a Monte Carlo simulation, accurately reflect reality? 3) What is the proton beam energy deposition profile along the axis of the target and from this energy profile can we determine the power being lost to wall interactions? And finally, 4) can we correlate this energy profile to radioisotope production yields?

The following chapter will describe the theory behind charged particle interactions in matter, particularly in regards to energy loss and scattering. It will also discuss the issue of beam density reduction and give the required background information for the production and decay of radioactive nuclides. Chapters 3 and 4 detail the experimental techniques used in this project. Chapters 5 and 6 present the results and discussion, respectively, and Chapter 7 reports on the conclusions we have drawn from our research.

Chapter 2
Theory and Literature of the Interaction of Charged Particles In Matter

2.1 Interactions of protons with matter

2.1.1 Energy Loss in Matter

Protons, as well as any charged particle whose rest mass greatly exceeds the rest mass of an electron, lose most of their kinetic energy through Coulomb interactions (inelastic collisions) with atomic electrons. This results in both ionization and excitation of the atoms in the absorber [17-18]. The original approach to evaluate this energy loss, developed by Niels Bohr in 1913 [19], was dependent on the impact parameter between the particle's trajectory and the target nucleus. However, with the advent of quantum mechanics, we must now consider that a particle with a well defined momentum cannot also have a well defined position. Thus, the approach most commonly used today, as developed by Hans Bethe in 1930 [20], depends on the momentum transfer from the particle to the target electrons [21].

For this project we have employed a Monte Carlo based program, the Stopping and Range of Ions in Matter (SRIM) [22], to model a proton beam incident on an Argon gas target. This section will provide an overview of the theory behind the stopping of heavy charged particles in matter.

The mean rate of this energy loss by ionization, also know as stopping power or specific ionization, can be approximated by the Bethe-Bloch equation:

$$-\frac{dE}{dx} = \frac{4\pi e^4 Z_2 Z_1^2 N}{m_e v^2}\left[\ln\frac{2m_e v^2}{\langle I\rangle} - \ln\left(1-\beta^2\right) - \beta^2 - \frac{C}{Z_2} - \frac{\delta}{2}\right] \qquad \textbf{[2.1]}$$

All variables, as taken from references 17, 18 and 21, are defined in Table 2.1.

Variable	Definition	Value
e	Elementary charge	1.602×10^{-19} C
Z_1	Particle atomic number	e.g.- proton $Z_1 = 1$
Z_2	Target atomic number	e.g.- carbon $Z_2 = 6$
m_e	Electron rest mass	5.11×10^5 eV
v	Particle velocity	Units given in meters per second.
I	Mean ionization energy of the atomic electrons	Usually regarded as an empirical constant.
C/Z_2	Shell Correction term	Experimentally determined. Only valid for particles with $Z_1 = 1$.
$\delta/2$	Density effect correction to ionization energy loss	Usually equal to zero for gases [12].
β	Relativistic particle velocity	Equal to v/c, were v is the incident particle velocity.
N	Atomic density of the target	Units given in atoms per cm^3.

Table 2.1: Definition of the variables found in Bethe-Bloch equation

A graph of the mass stopping power versus incident particle energy can be found in Figure 2.1. Linear stopping power is defined as the rate of energy loss per unit path length (MeV/cm), while the mass stopping power is this linear stopping power divided by the density of the absorbing material and is given in MeV/mg/cm^2. The values were determined using the SRIM computer program [22].

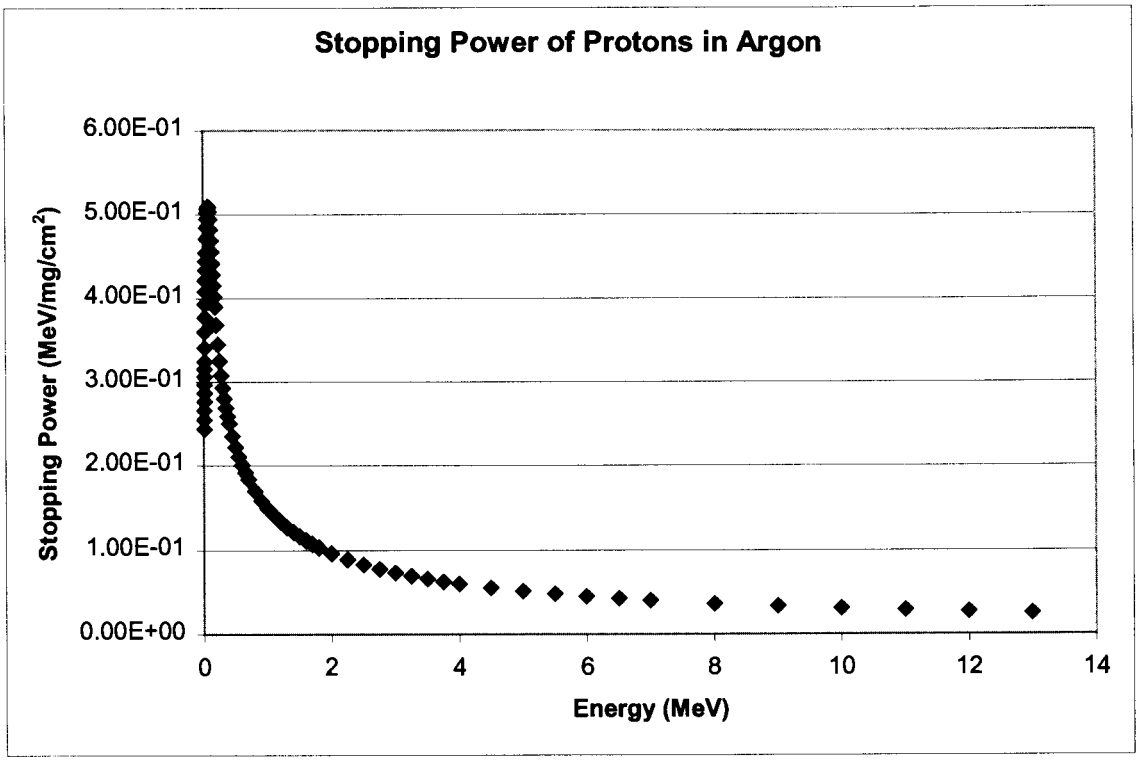

Figure 2.1: Mass stopping power as a function of incident particle energy for protons incident on Argon gas. The downward trend from approximately 100 to 0 keV is due to insufficient particle energy in order to overcome the binding energy of the target electrons.

This theory makes the assumption that the incident particle only interacts with the target through electromagnetic forces. All energy loss due to nuclear reactions is assumed to be negligible. It has been shown that less than 0.1% of the energy loss of high velocity particles can be attributed to the interactions with target nuclei [21].

The shell correction term, C/Z_2, compensates for the lack of participation of the inner shell electrons with the slowing down of the incident particle. The mean ionization term,

ln<I>, is the mean ionization potential needed to ionize the target atom electrons. The density effect term, $\delta/2$, corrects for polarization, which may occur in the target. As a proton passes through a target it can interact with many atoms at once and polarization of the target atoms along its path can occur thus reducing energy lost by the proton. This effect is dependent on the target density. Since the inter-atomic spacing in a gas is much larger than a solid or liquid the incident proton can only interact with one target atom at a time and the density effect term is assumed to be zero.

The total range of a particle, whose only mode of energy loss is through ionization and excitation of atomic electrons, can be found through the integration of the Bethe-Bloch equation above. This is known as the "continuous slowing down approximation" (CSDA) [18]. From this it follows that the range of a charged particle is affected by the following: the atomic number and mass of the target material, as well as the energy, mass and charge of the impinging charged particle [24].

2.1.2 Multiple Scattering

As mentioned above, the primary mode of energy loss between an incident heavy charged particle ($m>>m_e$) and the target material is through Coulomb interactions with the atomic electrons. A particle can interact with thousands of electrons along its track. This results in many small angle scatters and is known as multiple Coulomb scattering (or simply multiple scattering) [19]. Multiple scattering of the beam plays an important role in the design of gas target chambers. In a typical PET target body, a particle beam will pass through two thin foil windows, separated by helium cooling gas, prior to entering the target gas itself. Both foils as well as the gas will increase the angular spread of the beam and hence the location of deposited energy. In order to minimize loss of beam to the target body walls, many targets are designed to have a conical gas chamber to accommodate for this expansion in beam diameter [25-26].

The theory behind multiple scattering is very complex and there have been many attempts to explain and simplify it. The theory most commonly used today, was developed by Molière in 1948 [18-19, 27-28]. Molière theory uses small angle approximations to solve the general problem [19, 28]. To use this approach in a Monte Carlo simulation, however, would require a large amount of computational time and power. The SRIM Monte Carlo program makes use of a method developed by Ziegler, Biersack and Littmark (ZBL) as a simplification to this problem [22, 29-30]. The ZBL approximation makes use of Molière potentials and an analytic formula, referred to as the "Magic Formula" to determine the scattering angles [22, 29-30]. Its derivation can be found in references 29 and 30.

2.2 Gas density reduction

Gas targets are used extensively in the production of short-lived radioisotopes for radiopharmaceuticals due to their relatively simple design and the ease and speed with which the radioactivity can be transferred to the lab for processing. Gas targets, however, suffer from density reduction. This arises from heating of the gas by the particle beam. Because of this density reduction many research groups have witnessed an increase in particle penetration as well as a severe pressure rise with increased beam current [9, 14, 31-43]. For example, during a typical production run of Carbon-11 from Nitrogen gas, the initial gas pressure, prior to introducing the proton beam, is around 2172 kPa (315 psi). During bombardment with a 20 μA proton beam this pressure will then rise to approximately 2910 kPa (422 psi). Density reduction represents a severe hindrance on radionuclide yield because of gas molecules being forced out of the beam strike region by this pressure/temperature increase [3, 8, 32-34].

Heselius et al. [16] have studied this phenomenon by direct photography of the light emitted by target atoms during their bombardment with an intense ion beam. Figure 2.2 shows a 5.9 MeV deuteron beam incident on 960 kPa of Neon gas at 12 μA.

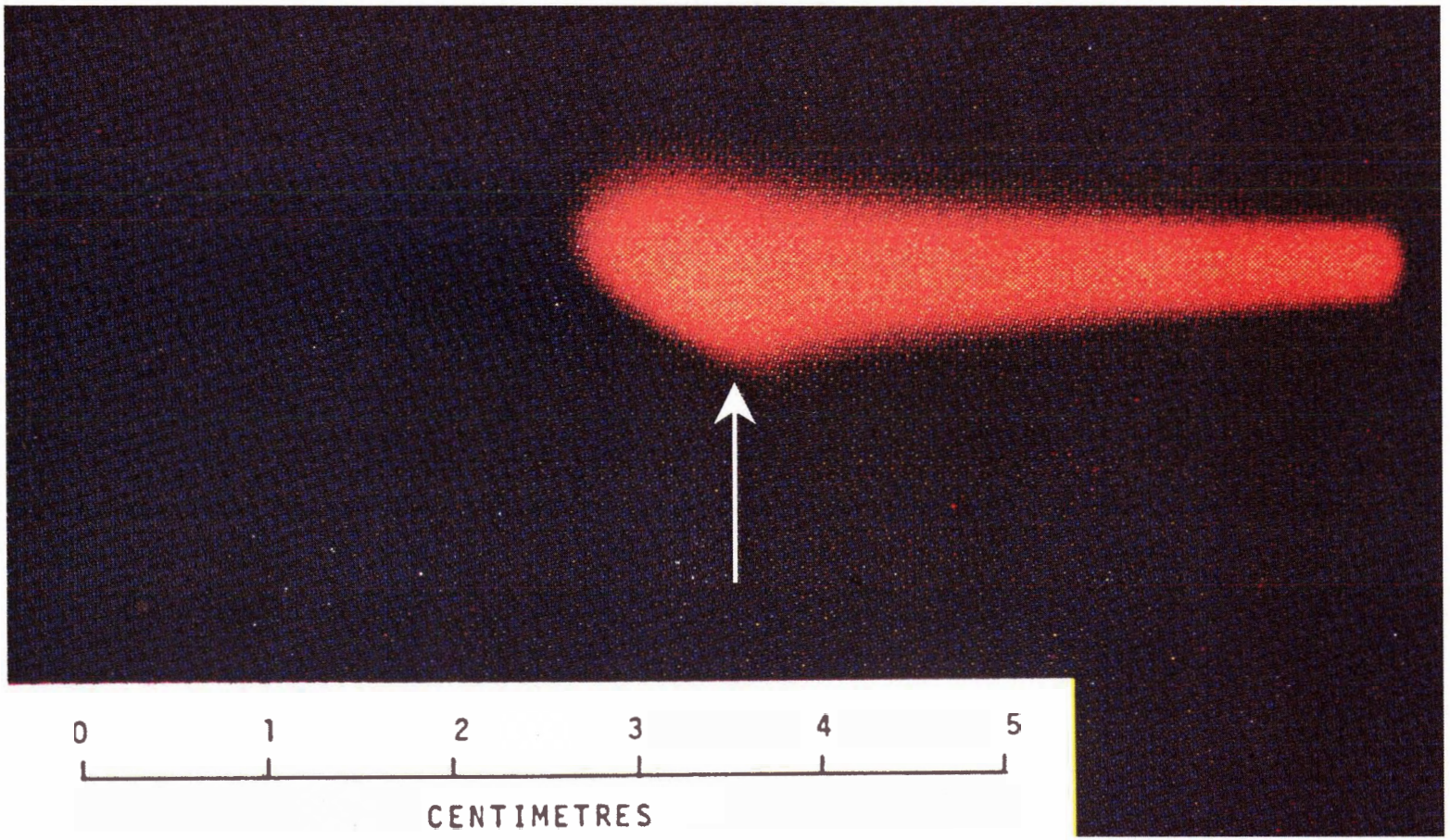

Figure 2.2: Photograph, taken by Heselius et al [16] of a 5.9 MeV deuteron beam incident on 960 kPa of Neon gas at 12 μA. The deuteron beam enters from the right hand side. Image courtesy of S.-J. Heselius.

Their target was 103 mm in length and was equipped with glass windows in order to view the beam. From this photograph we see an asymmetry in the beam shape. The bulge at the lower edge of the beam, indicated by the arrow, represents the theoretical range of the particles, however at this beam current the upper edge of the beam reaches substantially further into the gas due to a reduction in gas density in this area. This asymmetry is attributed to the upward thermal transport of the gas by heat deposited by the beam [16].

Many studies have been conducted into the research of density reduction. Still today, however, there is a struggle to run at high beam currents and achieve near theoretical yields. Some of these studies have included:

i. Interferometric readings of the gas density as a function of beam current [16]. The refractive indices found were then used to calculate the average temperature within the target.

ii. Particle penetration studies were performed via current produced across an electrically isolated exit window and beam stop placed at the end of a target [36]. The increase in particle penetration into the gas causes an increase in current reading as more charged particles penetrate the exit window.

iii. The pressure increase with increased beam current was also studied. The pressure-current relationship can be given by the following equation, $P=P_0(aI^b+1)$, found by Wojciechowski et al [44]. Here, P_0 and P are the initial and beam-on pressures respectively and "a" and "b" are regression constants. Using this, along with the ideal gas law, the change in gas temperature was estimated at $\Delta T=T_0(P/P_0-1)$.

2.3 Measuring the energy of protons

One of the objectives of this project was to obtain the energy of protons, which have been scattered to the outer walls of a gas target. This can provide insight into:

1. The amount of beam being lost because of scatter
2. The power being deposited into the walls; and
3. The effect of density reduction on beam distribution in the target.

The ultimate goal is to add to the already existing collection of knowledge on gas target systems in order to create an optimized target body with respect to shape, size and material.

In order to determine the energy of these scattered protons we have created a calibration curve of the ratio of the radioactivities of two simultaneously produced radioisotopes within a stack of copper foils versus the proton beam energy drop through each foil. The production of radioisotopes, as discussed in the following sections, changes as a function of energy. This calibration was determined by irradiating a stack of 15 copper foils, each 0.025 mm thick, and measuring the radioactivities of two isotopes produced with the use of a high purity Germanium detector. At 13 MeV, we will produce both Zinc-63 and Zinc-65 in natural Copper. The ratio of these radioactivities was then plotted as a function of the known energy drop through the stack of foils.

By lining the inner chamber of a gas target with similar copper foils and measuring the ratio of radioactivities produced after bombardment with the proton beam, we have been able to determine the energy of the scattered protons with our previous calibration. The following sections provide an overview of the theory behind radioisotope production and decay.

2.3.1 Radioisotope Production

Several common nuclear reactions for the production of PET isotopes can be found in Table 1.1. The probability that such a reaction will take place is dependent on the reaction cross-section, and hence incident particle energy, as well as the thickness of the

target in nuclei per cm^2 and flux of incoming particles. The rate of production is given by:

$$-\frac{dn}{dt} = R = nI(1-e^{-\lambda t})\int_{E_s}^{E_0}\frac{\sigma(E)}{dE/dx}dE \qquad \textbf{[2.2]}$$

Where:

R is the number of nuclei formed per second

n is the target thickness in nuclei per cm^2

I is the incident particle flux per second and is related to beam current

λ is the decay constant and is equal to $\ln 2/t_{1/2}$

t is the irradiation time in seconds

$\int_{E_s}^{E_0}$ is the integral from the initial to final energy of the incident particle along its path

$\sigma(E)$ is the reaction cross-section, or probability of interaction, expressed in cm^2

E is the energy of the incident particles

x is the distance traveled by the particle

Since the thickness of the copper foils used in this experiment is quite thin (0.025mm) we have assumed a linear change in cross section through each foil and hence used the average cross-section for the energy drop through each foil. This reduces the above equation to the following:

$$R=nI\sigma(1-e^{-\lambda t}) \qquad \textbf{[2.3]}$$

In our quest to map the energy with which our proton beam interacts with a gas target body's walls we have produced radioactivity in metal foil linings. As mentioned above the amount of radioactivity produced is dependent on the cross-sections for the nuclear

reaction in question. Cross-sections for nuclear reactions are highly dependent on the energy of the incident particle. This dependence is referred to as the "excitation function" of a particular reaction [17, 24]. As an example, the excitation function for the production of Carbon-11 from Nitrogen-14 can be found in Figure 2.3 below. Classical theories on nuclear reaction cross-sections simply utilize the geometrical area of the target nucleus (πR^2), so long as the incident particles energy was sufficiently large to overcome Coulombic repulsion [17]. It follows that the units for a cross-section are those of area and are called *barns*, where 1 barn = 10^{-24} cm^2 [17, 20, 24, 45].

Most charged particle reactions are referred to as "threshold reactions" [24]. This is because the charged particle must have a minimum energy in order to overcome the Coulomb barrier of the nucleus it is impinging upon as well as reserve some of it's energy to conserve the momentum of the system. Interactions below the threshold energy, however, do sometimes take place through quantum-mechanical tunneling [24]. Considering Figure 2.3 we can see that the threshold energy for the reaction ($^{14}N+p \rightarrow {}^{11}C+\alpha$) is around 4 MeV.

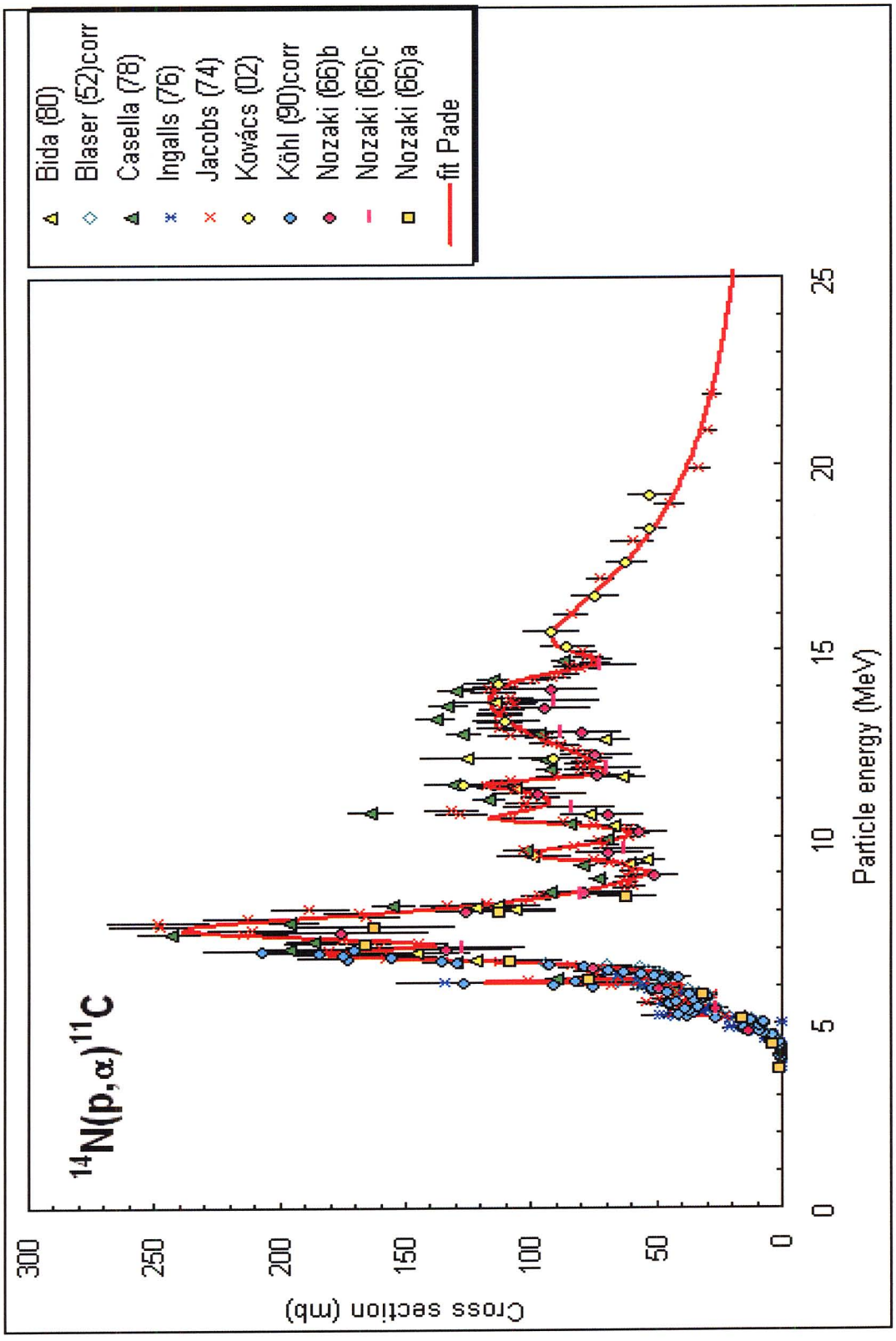

Figure 2.3: Excitation function for the production of ^{11}C from ^{14}N. Published in [46].

2.3.2 Radioactive Decay

Radioactive decay is a spontaneous, statistically random process whereby particles or electromagnetic radiation are emitted during a nuclear transition [17, 20, 24]. During this process a radionuclide, called the parent, emits particles to form an entirely new isotope, called the daughter. The daughter may be either stable or radioactive. The most common modes of decay are through alpha, beta, including electron capture, and gamma emission. The rate with which a radioisotope will decay, measured in disintegrations per second, is simply the radioactivity given by [17, 20, 24]:

$$A = A_0 e^{-\lambda t} \qquad \textbf{[2.4]}$$

Where:

A is the radioactivity in disintegrations per second

A_0 is the initial radioactivity at t = 0

λ is the decay constant and is equal to $\ln 2/t_{1/2}$, where $t_{1/2}$ is the half-life of the isotope in seconds.

And t is the time the radioisotope has decayed, in seconds.

An isotope may decay by one or more decay modes. This is called branching decay. The transition from the parent to daughter isotope can be described using a "decay scheme". Figure 2.4, adapted from reference 47, shows the decay of Zinc-65 to Copper-65 through electron capture, a form of beta decay: $^{65}Zn + e^- \rightarrow {}^{65}Cu^* \rightarrow {}^{65}Cu + \gamma$.

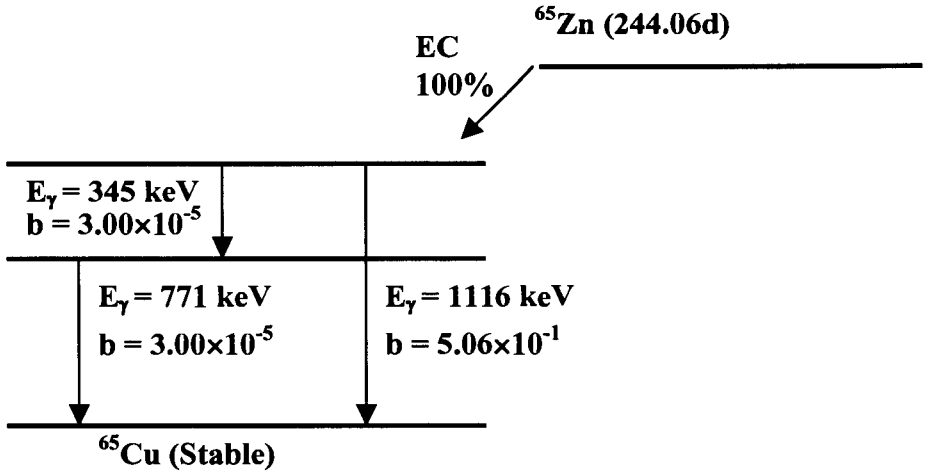

Figure 2.4: Decay scheme for Zinc-65. E_γ is the γ-ray energy and b is the branching ratio. Adapted from [47].

We can see from this decay scheme that Zinc-65 decays to an excited state of Copper-65. Copper-65, in turn, emits photons during its transition to the ground state. These photons are emitted at known energies with known branching ratios. Therefore, when we observe spectra of these gamma emissions, which are discussed in Chapter 3, we are observing the photons emitted by Copper-65 as a result of the decay of Zinc-65.

Chapter 3
Experimental Techniques Part I.
Proton Scattering in Gas Targets

3.1 Theoretical Proton Scattering in a Gas Target Using a Monte Carlo Model.

As discussed in Section 2.1.2, theory suggests that a proton beam incident on a gas target should be primarily forward directed with a slight beam expansion due to scatter, as illustrated in Figure 3.1, and this effect should not be dependent on the number of protons incident on the target gas.

A Monte Carlo based program, SRIM (the Stopping and Ranges of Ions in Matter), was employed in order to model the theoretical attenuation and scattering of a beam of protons entering a gas target. As a charged particle passes through a target material it can interact with each target atom along its path. A number of events can occur during interaction ranging from elastic scattering, where the incident particle emerges with the same energy, to ionization of a target electron, to even nuclear reactions. The likelihood of each interaction has a probability function for that event. The usefulness of the Monte Carlo technique arises from its ability to randomly select which event will occur based on each interactions probability function. Each particle is tracked along its path until it is stopped in either the gas or the target chamber walls.

SRIM allows the user to choose the number and type of ions incident on the target, as well as the target material, state, and pressure. The program will then output, both graphically and in text lists, the x, y and z coordinates of each interaction of a proton with a gas molecule as well as the energy with which the proton interacts.

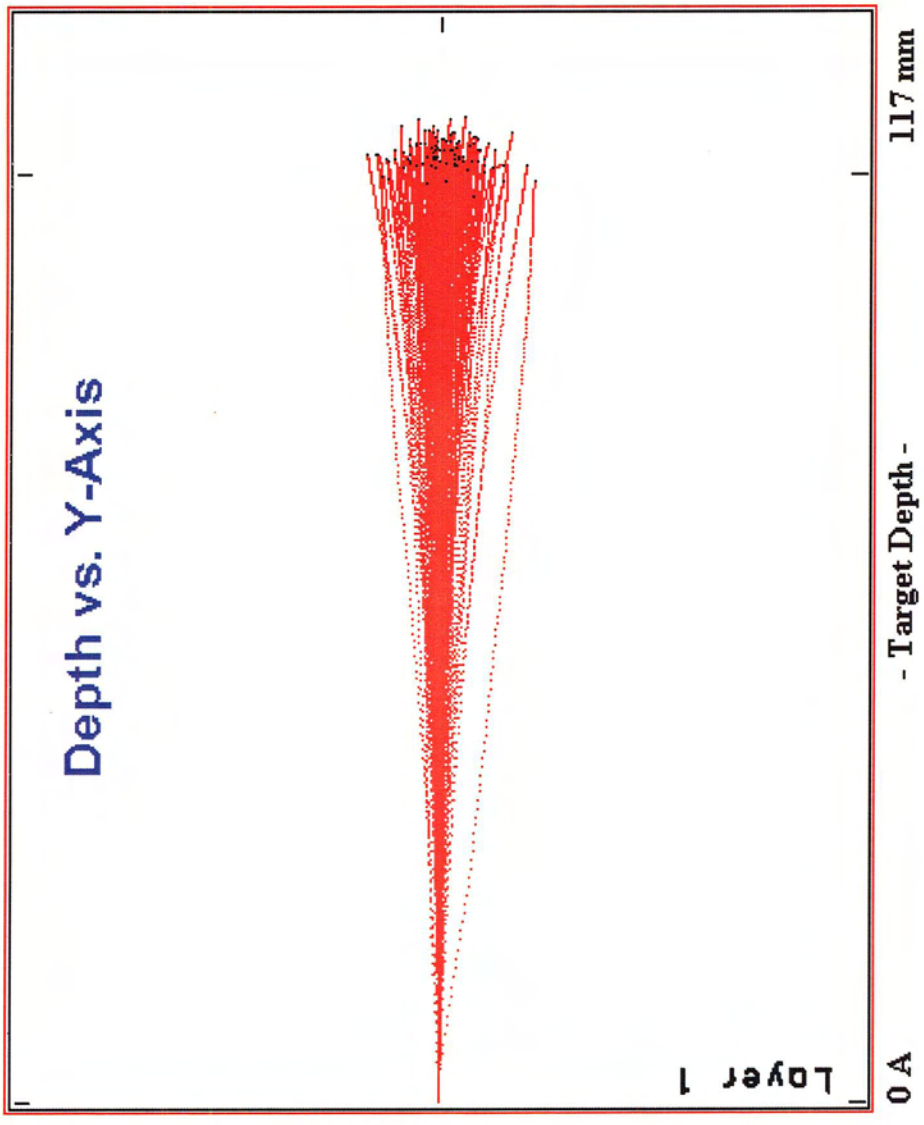

Figure 3.1: Graphical output from SRIM depicting 12.5 MeV H ions incident on Argon gas at 1551 kPa (225 psi). The y-axis illustrates the spatial distribution. The proton beam enters the target gas from the left.

In order to determine the theoretical energy with which a beam of protons should be interacting with our experimental target body walls, a program was written using Microsoft Visual Basic™. This program takes the SRIM text file as input, which consists of lists of the x, y, and z coordinates and the energy of the proton at each of these positions and then calculates the magnitude of the vector between the x and y coordinates of each interaction by the equation:

$$\overline{V} = \sqrt{x^2 + y^2} \qquad \textbf{[3.1]}$$

By setting this vector equal to the radius of our target's inner chamber, r = 7.5 mm, we can pick out the energy of the interacting proton at that radius. These energies are then averaged over intervals along the length of the target, corresponding to the experimental portion of this project.

For this model Argon gas was used at 690 kPa (100 psi), 1551 kPa (225 psi) and 2068 kPa (300psi). These pressures were chosen to mimic a thin, borderline thick and thick target. A gas target is said to be thick if the number of gas molecules within the beam's path is high enough to reduce the incident particle's energy to below the threshold energy of the reaction in question. Conversely, a thin target results from a lack of sufficient amounts of gas molecules to reduce the beam energy to below this threshold. A borderline thick target, hence, would allow the protons to just reach the end of the target with the reaction's threshold energy. A discussion of cross-sections and threshold energies can be found in Section 2.3.1.

At low beam currents this model should accurately describe the proton beams interaction with the target gas, however, since the SRIM Monte Carlo program is not designed to model thermal effects the model is expected to fail with increased beam current. This project was aimed at studying this deviation from the low current baseline.

3.2 Imaging Proton Scattering in a Gas Target using Autoradiography.

In order to qualitatively view that the theoretical model above does not adequately describe what is taking place within our experimental gas target we have employed autoradiographic imaging.

The autoradiography system at the Brain Research Center at The University of British Columbia Hospital is a Cyclone® storage phosphor system. It consists of a set of phosphor crystal plates and a laser scanner, as seen in Figure 3.2.

Figure 3.2: Cyclone® storage phosphor system and phosphor screens. Image Courtesy of PerkinElmer, Inc.

Radiographic images are acquired through a storage phosphor process, as described in Figure 3.3. Radioactive samples are placed onto the Europium doped crystal plates ($BaFBr:Eu^{2+}$). As the sample activity decays, the particles emitted ionize the Eu^{2+} to Eu^{3+}. This liberates electrons to the conduction band of the crystal. Once the radioactive sample is removed, exposing the plates to red laser light at 633 nm will cause the Europium to emit a photon at 390 nm in order to return to its ground state [48]. These

photons are collected and plotted by the scanner and the OptiQuant™ image analysis software, in order to recreate an image of where the activity was previously placed.

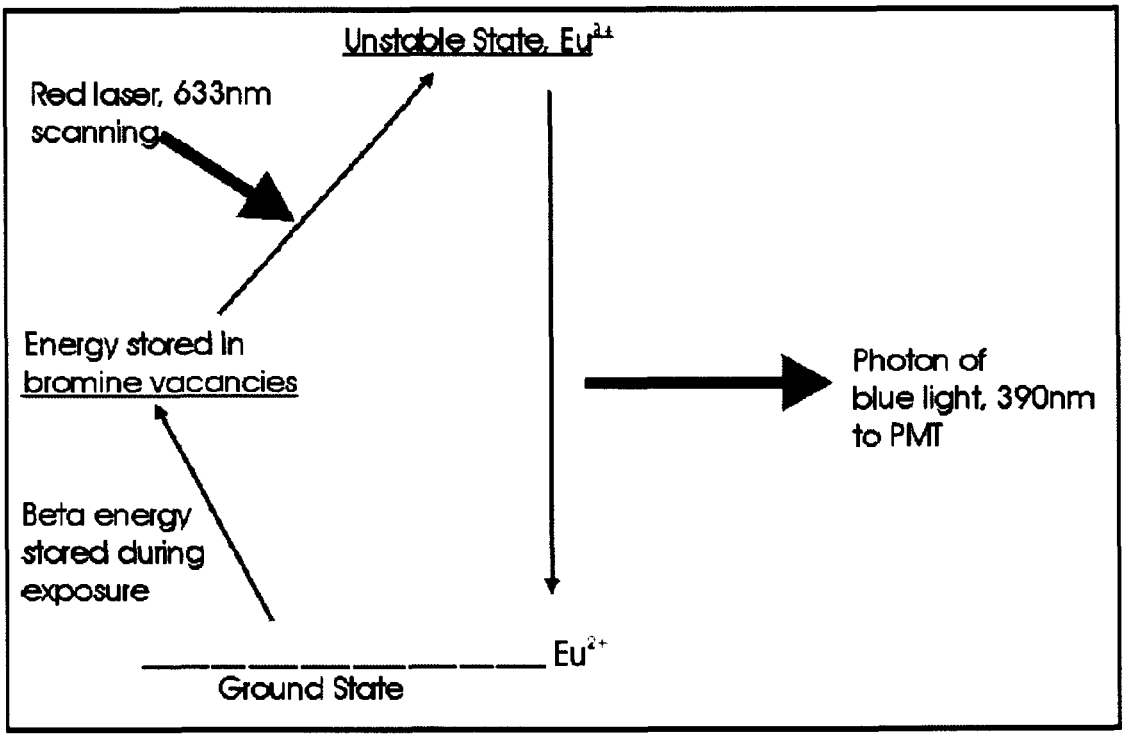

Figure 3.3: Schematic representation of the storage phosphor process. Image courtesy of PerkinElmer, Inc.

In order to indirectly image the protons interacting with the inner wall of our experimental target we have imaged the radioactivity produced in a copper foil lining by the scattered protons. The production of activity in metal foils has previously been described in Section 2.3. A schematic drawing of the experimental target can be found in Figure 3.4.

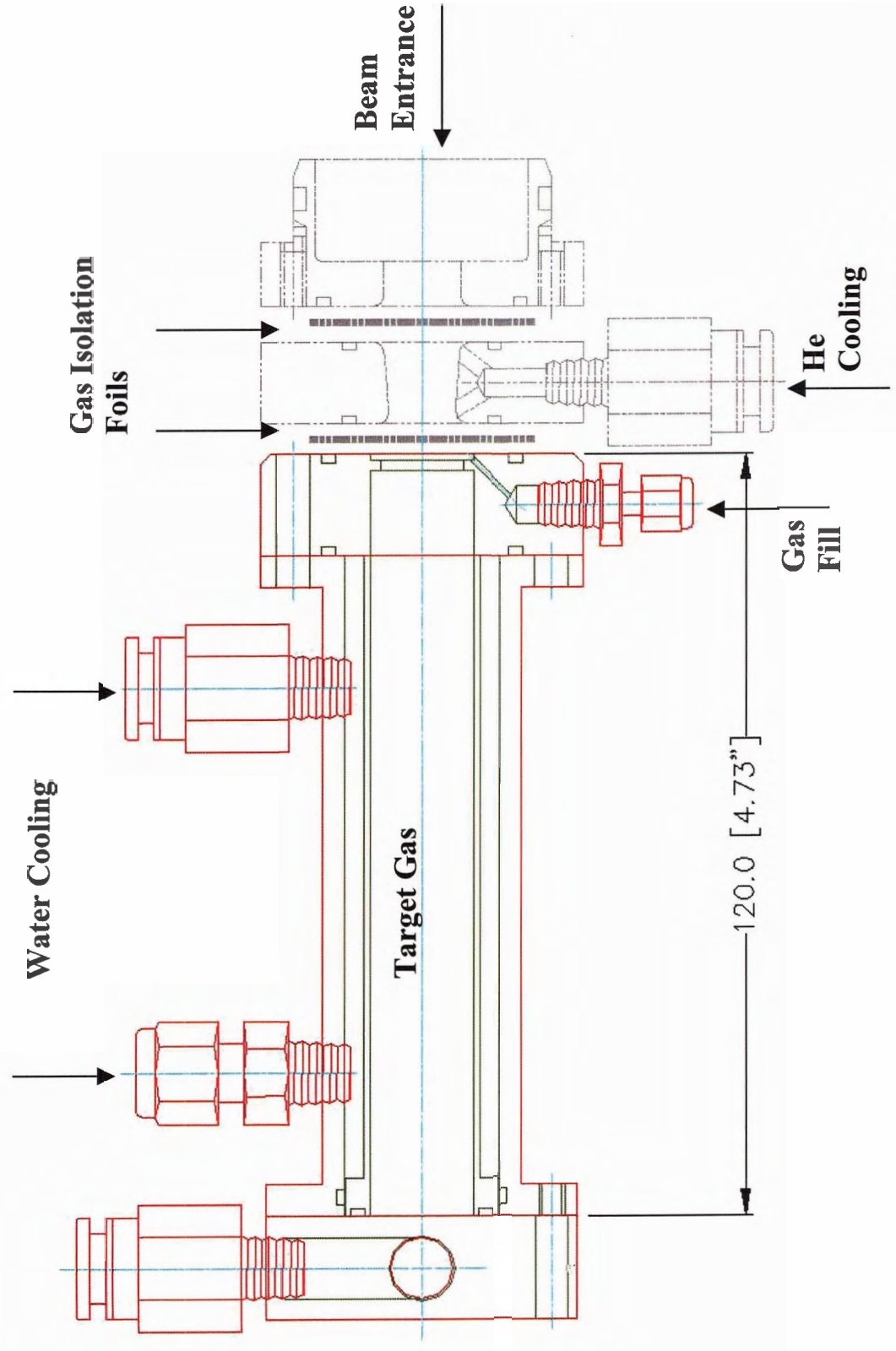

Figure 3.4: An AutoCAD™ schematic drawing of the experimental gas target. The inner diameter of the gas chambre is 7.5 mm.

Chapter 4
Experimental Techniques Part II. Energy Mapping of Scattered Protons Interacting with Gas Target Body Walls

4.1 Stacked Foil Irradiations

From the theory presented in Chapter 2 we can see that we should be able to calculate the energy of the particles, which are scattered to the target body walls, by measuring the radioactivity produced in a foil liner. This radioactivity could then be used to simply calculate the cross-section that would be needed to produce such radioactivity and from the cross-section we could determine the energy of the particle directly from the excitation function for that reaction. To do this, however, we would need accurate knowledge of the flux of the particle beam. That is, we would need to know the exact number of particles being scattered to the walls. This is a difficult question to answer; therefore, we have developed a technique to overcome this obstacle.

In order to obtain the energy of the protons interacting with the target body walls we employed a stacked foil technique to create a calibration curve of the ratio of radioactivities of two simultaneously produced isotopes versus the energy drop through each foil. We then used this calibration curve to determine the proton energy simply by the activity produced in a foil lining.

To generate our calibration curve, a stack of 15 copper foils, each 0.025 mm thick, was placed perpendicular to the proton beam. A schematic of the target holder can be seen in Figure 4.1. As the proton beam passes through each subsequent foil its energy is decreased. This decrease can be estimated by stopping range tables, as provided by the SRIM computer program [22]. These ranges are dependent on the stopping power, dE/dx, of the copper foils. The results of a 12.8 MeV beam through our stack of copper foils can be seen in Table 4.1.

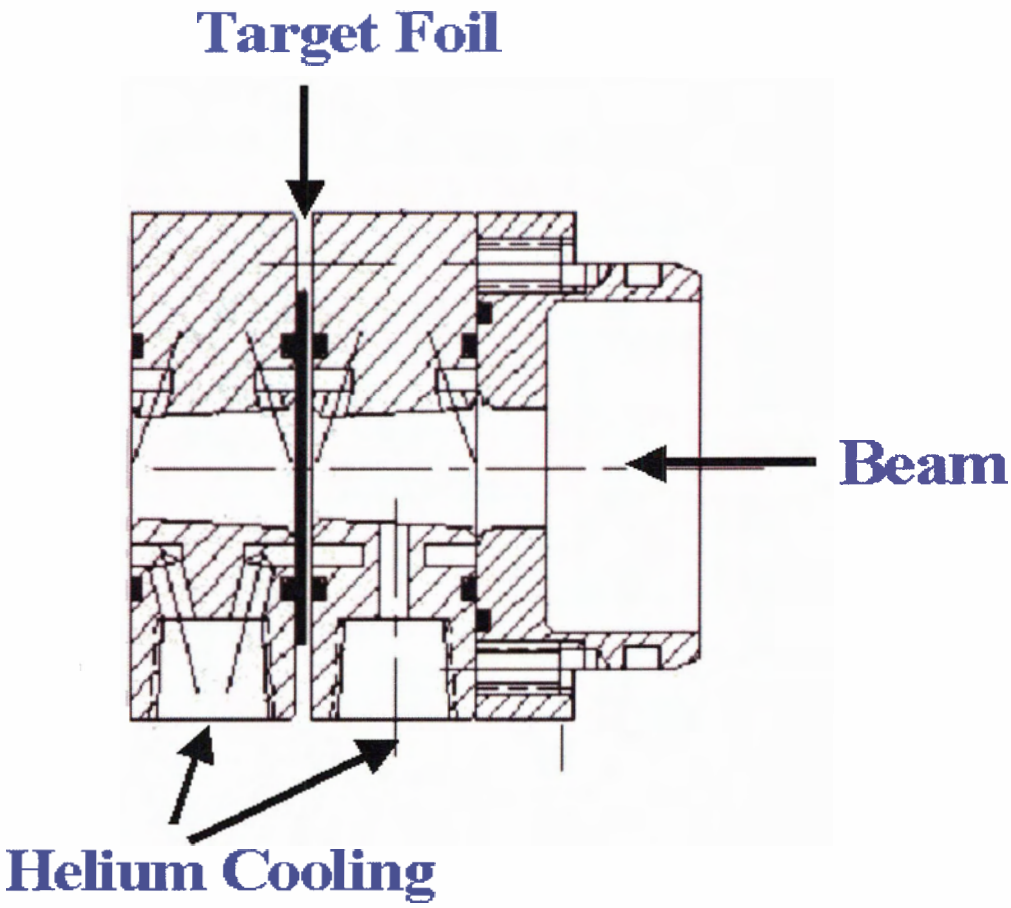

Figure 4.1: Schematic drawing of the holder used during irradiation of the target foils. The Helium cooling exit ports are not visible in this view.

Foil number	Energy of Proton beam entering the foil (MeV)	ΔE (MeV)
1	12.8	0.6
2	12.2	0.5
3	11.7	0.6
4	11.1	0.6
5	10.5	0.6
6	9.9	0.6
7	9.2	0.7
8	8.5	0.7
9	7.8	0.7
10	7.0	0.8
11	6.1	0.9
12	5.2	0.9
13	4.2	1.0
14	2.9	1.8
15	1.1	1.1- threshold energy

Table 4.1: Proton range table through 15 copper foils, each 0.025 mm thick.

The resolution of the calibration is limited by the thickness of the foils. As the protons pass through a single foil, their energy decreases by a finite amount. This amount increases with foil thickness. As a result, each foil actually represents a range of energies, from the protons entrance energy to their exit energy.

Copper has two naturally occurring isotopes, ^{63}Cu and ^{65}Cu. During bombardment with 13 MeV protons we produce both ^{63}Zn and ^{65}Zn through (p, n) reactions. Table 3 lists the relevant parameters for these reactions.

Natural Copper	Percent Abundance	Reaction	Product	Half-life
^{63}Cu	69.17%	^{63}Cu(p,n)^{63}Zn	^{63}Zn	38.47m
^{65}Cu	30.83%	^{65}Cu(p,n)^{65}Zn	^{65}Zn	244.06d

Table 4.2: ^{nat}Cu(p,n)^{63,65}Zn parameters.

The radioactivity of each radioisotope was determined with the use of a high purity germanium detector (HPGe). Figure 4.2 shows a sample gamma spectrum of one of the foils. The peaks used in the calculations, labeled at 962.1 keV and 1116 keV, correspond to the decay of ^{63}Zn and ^{65}Zn respectively. All unlabeled peaks are also accounted for by the known gamma-rays of the two isotopes. A brief overview of the HPGe detector used in this project along with an explanation of the efficiency and energy calibrations performed can be found in appendix A.

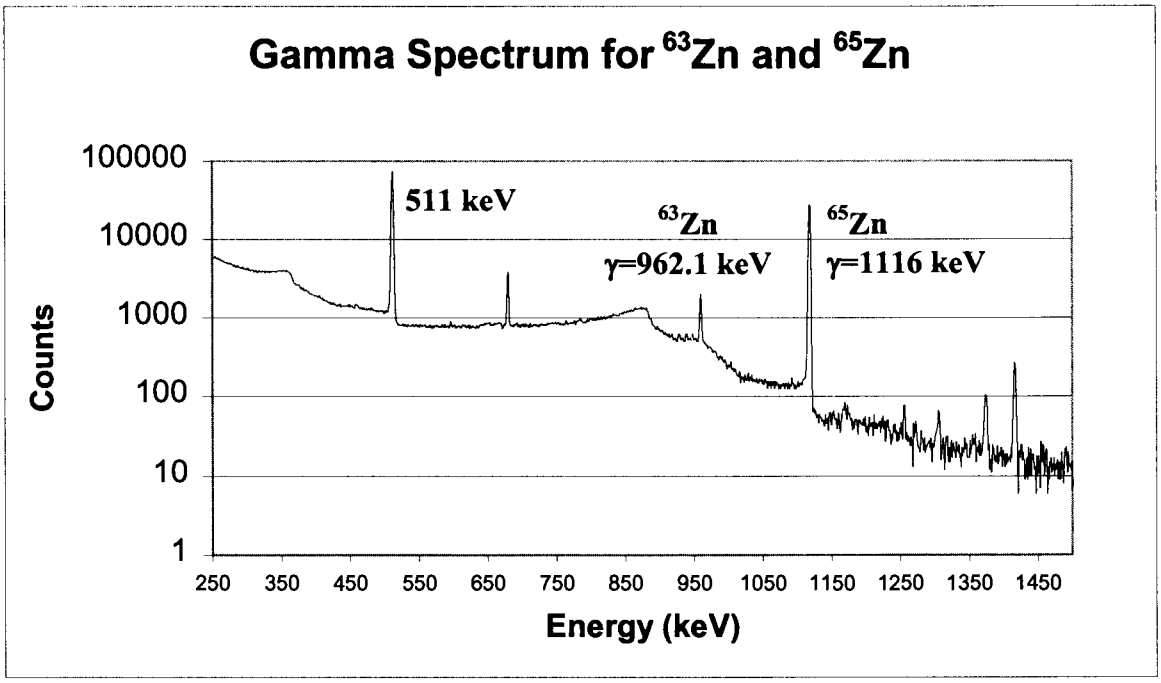

Figure 4.2: Gamma spectrum of an irradiated Copper foil. All unlabelled peaks are accounted for by the gamma-rays of the two Zinc isotopes. The large peak at 670 keV is from the decay of ^{63}Zn. The baseline is due to photons, with a continuum of energies, which arise during Compton interactions. The peak at 511 keV is due to the annihilation photons which arise as a result of positron decay of the two isotopes and pair production in the detector crystal. The "jitter" is due to statistical fluctuations in counts at low total counts.

The number of counts from each peak is related to the activity of the isotope by the equation:

$$A = \frac{dN}{dt} = \frac{n}{b\varepsilon t} \qquad [4.1]$$

Where:

dN/dt is the activity of the isotope in disintegrations per second

n is the number of counts

b is the branching ratio for that peak,

see section 2.3 for more information on decay schemes,

ε is the efficiency of the detector at that energy and geometry.

See Appendix A for details.

and t is the detector counting time, in seconds.

As the energy of the beam decreases, the activity produced in the foils will vary due to the changing cross-section of the two reactions $^{63}Cu(p,n)^{63}Zn$ and $^{65}Cu(p,n)^{65}Zn$. Cross-section theory can be found in Section 2.3.1

The activity of each isotope produced during bombardment can be calculated using equation 2.3:

$$R=\frac{dN}{dt}=nI\sigma(1-e^{-\lambda t}) \qquad \textbf{[4.2]}$$

Because the calibration curve made use of the ratio of the activities for each isotope, error incurred through fluctuations in beam current is factored out, leaving the only opportunity for experimental error in irradiation times. Also, using an experimental calibration curve instead of one calculated from theory eliminates the uncertainty in the literature values for the cross-sections. If the values for the cross-sections used are those for natural copper the number of target atoms is also eliminated from the ratio since the natural abundances for the two stable isotopes has already been accounted for. The ratio can be seen below where the subscripts 1 and 2 indicate variables corresponding to ^{63}Zn and ^{65}Zn, respectively.

$$Activity\ Ratio = \frac{A_1}{A_2} = \frac{nI\sigma_1(1-e^{-\lambda_1 t})}{nI\sigma_2(1-e^{-\lambda_2 t})} = \frac{\sigma_1(1-e^{-\lambda_1 t})}{\sigma_2(1-e^{-\lambda_2 t})} \quad \textbf{[4.3]}$$

4.2 Foil Lined Gas Target

The experimental target, corresponding to the schematic in Figure 3.4, can be seen in Figure 4.3.

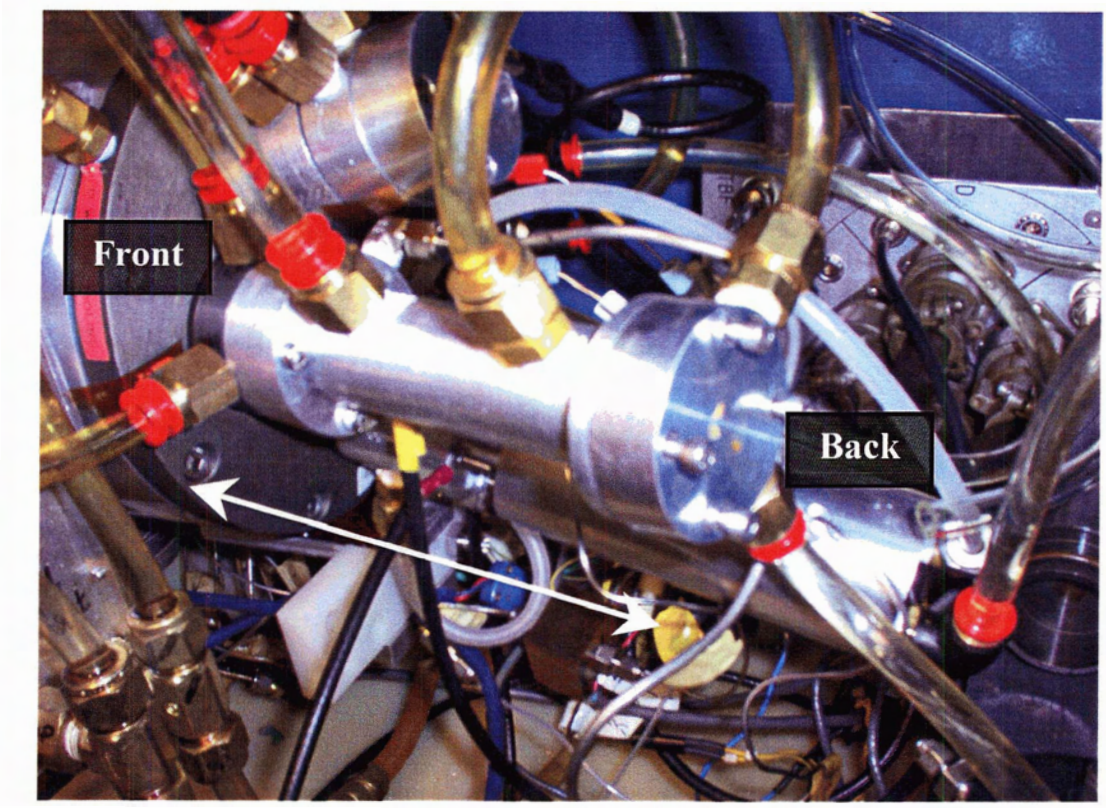

Figure 4.3: Photograph of the experimental gas target. The proton beam enters from the left. The rear panel is removable to allow for the insertion of a copper foil lining. The target is approximately 150 mm in length.

A rectangular copper foil lining, with dimensions of 12 cm by 5 cm, is inserted through the rear and the back panel is lined with another small circular foil. The chamber is then sealed and filled with Argon gas. The target is then irradiated for 5 minutes and the

radioactivity is allowed to decay for a sufficient amount of time in order to minimize personal radiation dose exposure. These decay times are 1 h for each 1 μA run, 3 h for each 10 μA run and 4 h for each 20 μA run. This is repeated for each of the beam currents and pressures found in Table 4.3.

Initial Target Pressure (kPa ± 20 kPa)	**Beam Current (μA ± 0.5 μA)**	**Irradiation Time (minutes ± 2 seconds)**
690	1, 10	5
1551	1, 10, 20	5
2068	1, 10, 20	5

Table 4.3: Irradiation parameters used during experimental gas runs.

After irradiation the Argon gas is released to a sealed bag to avoid possible air contamination with radioactive gas. The foil liner is then removed from the target body and cut into 12 equal size pieces. See Figure 4.4 below for details.

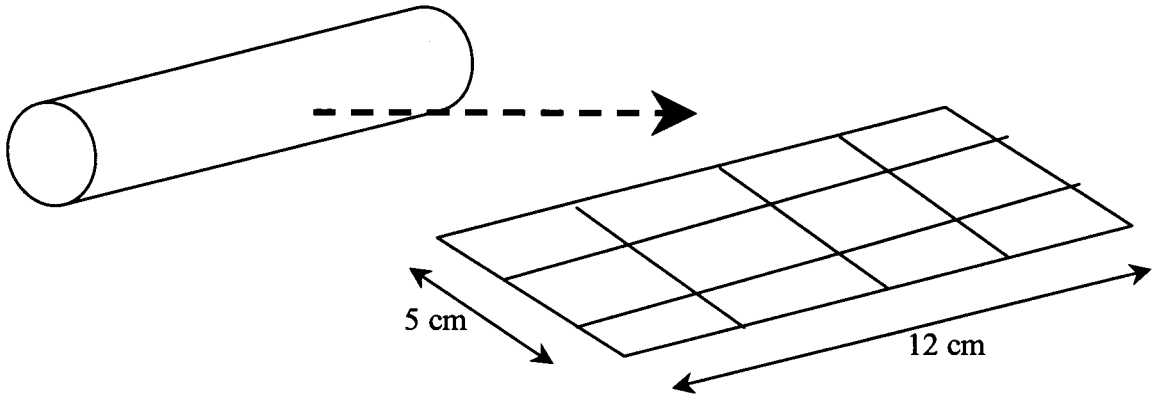

Figure 4.4: The Copper foil is initially rolled into a cylinder to line the target body walls. After removal the foil is unrolled and cut into 12 equal size pieces.

The activity produced in each piece, including the rear liner foil, is determined using the HPGe detector, and the radioactivity of each isotope is calculated as describe in Section 4.1. Once we have obtained the ratio of the activities of the two isotopes for each section of the foil liner we determine the corresponding proton energy from the energy calibration curve in Figure 5.3.

Chapter 5
Results

5.1 Monte Carlo Model for Proton Scattering

The results for the Monte Carlo model can be found in Table 5.1. The top number in each cell is the average energy of the protons interacting with the target body walls. The bottom number is the relative number of proton interactions with the walls in each depth interval. This has been normalized to the number of interactions determined for the depth having the maximum number of interactions. These intensities have been plotted as a histogram and can be found in Figure 5.1.

Pressure / *Depth*	***690 kPa***	***1551 kPa***	***2068 kPa***
0-3 cm	11.1 MeV 0.001	9.5 MeV 0.003	9.0 MeV 0.005
3-6 cm	10.1 MeV 0.043	7.5 MeV 0.039	5.0 MeV 0.139
6-9 cm	9.1 MeV 0.298	3.6 MeV 0.476	1.0 MeV 1
9-12 cm	8.0 MeV 1	0.5 MeV 1	- 0
Back of Target	7.5 MeV 0.1424	- 0	- 0

Table 5.1: Monte Carlo model of proton energy interacting with a gas target body. Note theory indicates a symmetric beam shape. The top number is the average proton energy. The lower number is the relative number of proton interactions and has been normalized to the number of interactions for the depth with the maximum number of interactions.

The depth intervals correspond to the size of the cut foil pieces in the experimental portion of this project. To correct for the finite spatial distribution of the experimental proton beam the program was run for a target radius of 0.75 cm (1.5 cm diameter target chamber) and then again for a target radius of 0.25 cm. The results for r = 0.75 cm and r = 0.25 cm were averaged in order to mimic a beam spot size of 1 cm diameter. These

numbers were calculated based on 2,000 incident protons; 1000 originating from the centre and 1000 at 0.5 cm from the centre (i.e. 0.25 cm in from the target wall, hence the 0.25 cm radius calculations). As a comparison the SRIM program was run using 10,000 incident protons at 2068 kPa and resulted in a variation in one decimal place of the energy. The error quoted from the SRIM documentation is on average 7% [29].

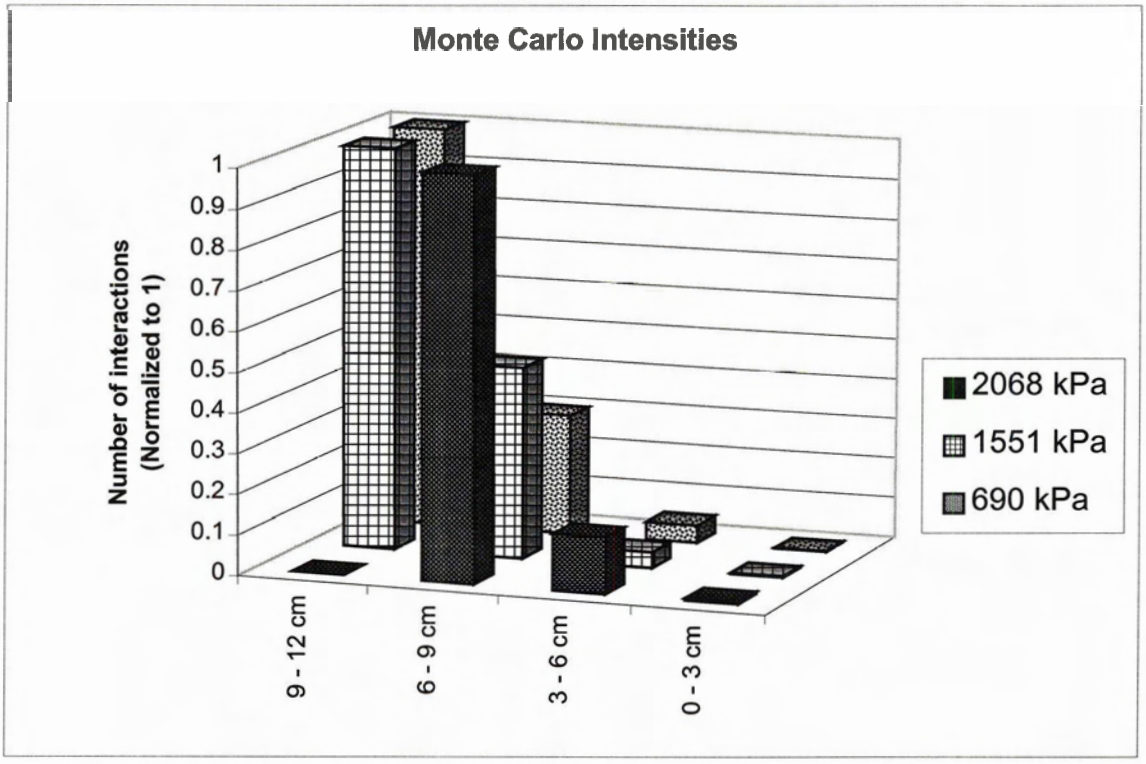

Figure 5.1: Relative proton intensities for 690, 1551, and 2068 kPa are given. The proton beam enters from the right hand side. Only the variation in intensity with depth is given. Theoretical particle scattering predicts a uniform beam expansion and therefore no radial variation in proton intensities.

5.2 Autoradiographic Images of Radioactivity Produced in a Copper Foil Lining

The results from the autoradiographic images of the copper foil lined gas target can be seen in Figure 5.2.

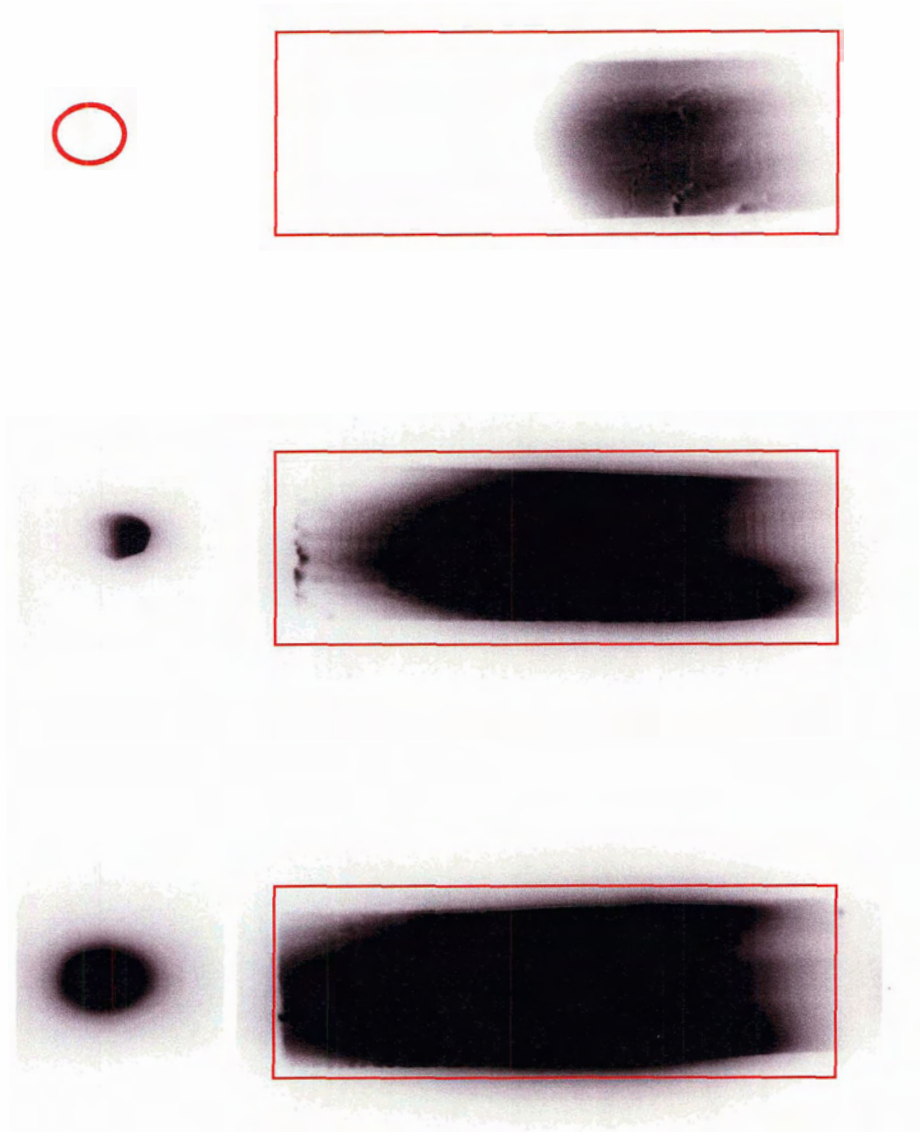

Figure 5.2: Autoradiographic images of induced radioactivity in the Copper foil linings as a result of proton interactions with the foil. Argon gas was used at an initial pressure of 2068 kPa (300psi). The beam currents, from top to bottom, are 1μA, 10μA, and 20 μA. The foil dimensions (indicated by the box) were 5 cm by 12 cm. The foil lining the back was 1.5 cm in diameter. The foil orientation during irradiation was with the central axis of the foil along the top of the cylindrical target body and the edges of the foil met at the bottom of the target body. The proton beam entered from the right hand side.

The foil lining was rectangular in shape. This rectangle was rolled into a cylinder and slid into the cylindrical target body. The orientation of the foil is such that the central axis of the rectangle was placed along the top of the target while the outer edges met at the bottom of the target. A separate circular foil was used to line the back. In these images the proton beam is entering from the right hand side. The boxes drawn around the images are to indicate the edges of the foils and the circle in the top image is to indicate the absence of activity in the foil lining the back of the target at 1 μA. As we progress from 1 to 20 μA, we clearly see the increase in proton penetration which we hypothesize is due to density reduction in the gas.

5.3 Calibration curve

The calibration curve can be seen in Figure 5.3, as well as a theoretically calculated curve, which was determined using equation 4.3 and published cross-sections [49]. Each point on the experimental curve corresponds to one foil in the stack of 15 Copper foils. The x-error bars given are simply the energy drop through that foil. The SRIM documentation reports an additional error of approximately 7%. The y-error was calculated with consideration to the errors associated with irradiation time, counting statistics and geometric efficiency (discussed in Appendix A). The maximum variation in irradiation time was taken to be 2 seconds, giving an associated error of 1.75%. The uncertainty in the counting statistics was taken to be the square root of the number of counts recorded by the Germanium detector. Since the error belonging to the calibration source used in the calculation of the efficiency (see Appendix A) curve was not known a maximum uncertainty of 5% was used. This more than compensates for the uncertainty associated with the counting statistics (< 2%) during the calibration. The deviation between experimental and the calculated values in the lower portion of the curve can be explained by energy straggling. Energy straggling is a result of the statistical nature of charged particle energy loss. As a beam of particles pass through a finite thickness of absorber they are no longer monoenergetic, but have a distribution of energies about the predicted energy. The published cross-sections used in the calculated curve drop to zero

around 4 MeV, the proton beam, however, contains particles above and below this value so that even though the average proton energy may be below the threshold for the nuclear reaction there are still protons present with sufficient energy to overcome this threshold.

Because of the large flat region on the calibration curve we essentially only have 5 regions of discernable energies: from 0 to 1.1 MeV, from 1.1 to 2.9 MeV, from 2.9 to 11.7 MeV, from 11.7 to 12.2 MeV and from 12.2 to 12.8 MeV.

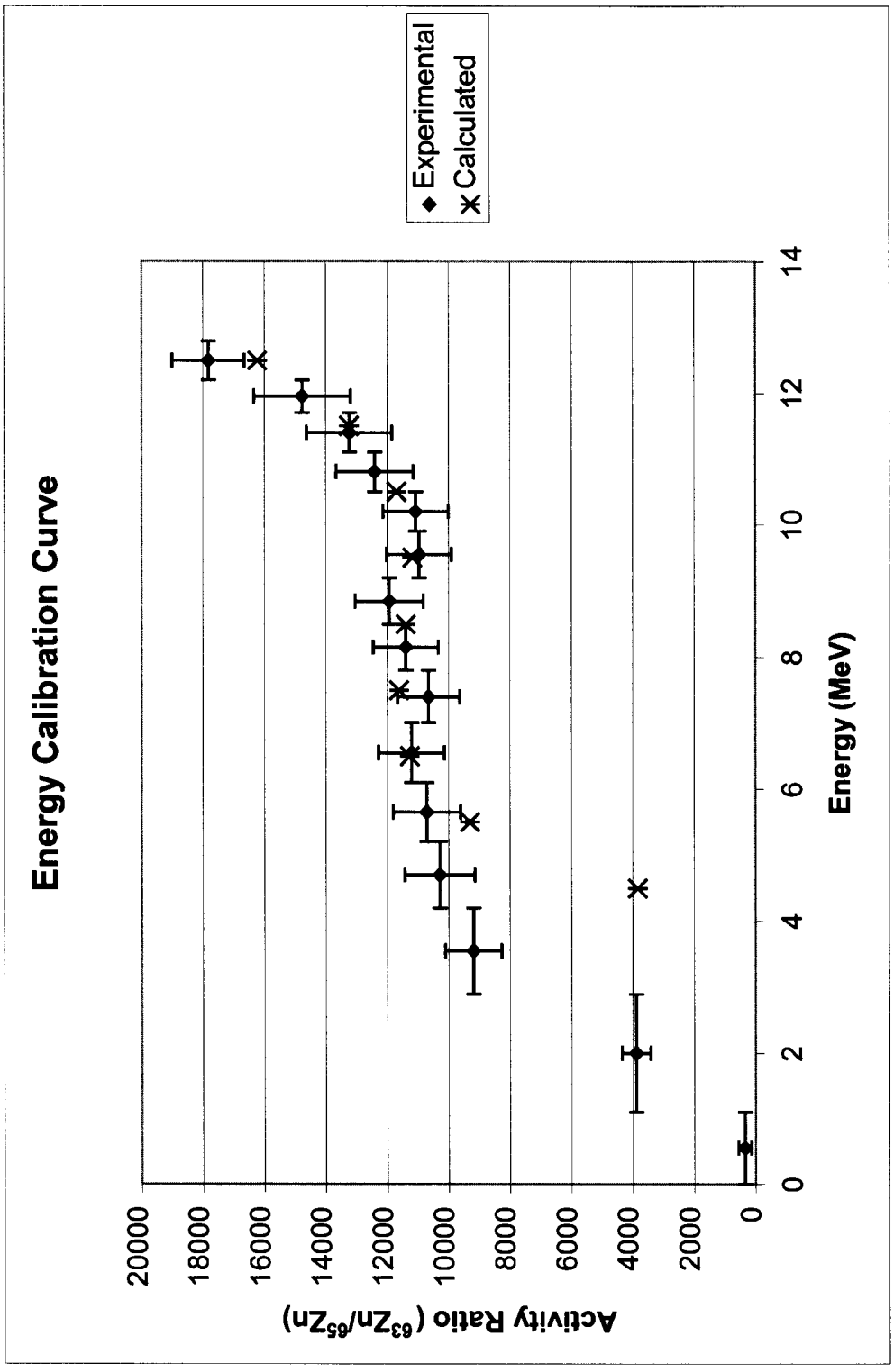

Figure 5.3: Calibration curve of the activity ratio of Zinc-63 to Zinc-65 versus energy.

5.4 Foil Lined Gas Target

The results for the each pressure can be found in Figures 5.4 to 5.6. Tables of the results for each of the three pressures can also be found in Appendix B. The proton beam enters from the right hand side. The grid represents the cut foil pieces and the box to the left is the liner for the back of the target. The top data set, for 1μA, is marked with the corresponding depth intervals according to the cut copper foil lining. All other data sets have the same intervals. Within each box, representing one cut foil segment, are 3 numbers. The top number, in bold lettering, is the energy range according to the calibration curve, in MeV. The middle number is the calculated radioactivity ratio for the two isotopes. The final number is the radioactivity for Zinc-65. The radioactivity has been normalized to the measured radioactivity for the cut foil segment having the highest radioactivity level for a given run.

Histograms of the radioactivity of Zinc-65 in each foil segments have been plotted and can be found in Figures 5.7 through 5.9. It should be noted that the general trend seen in the Zinc-65 data sets was the same for the Zinc-63 data sets. The asymmetry of beam deposition in the foil lining can be seen in these figures. The lower activities in the right hand side of the foil is due to a slight overlap of the left side of the foil.

1 μA at 690 kPa

2.9-11.7 MeV 10283 1	**2.9 - 11.7 MeV** 9344 0.22	**2.9 - 11.7 MeV** 9845 0.21	**2.9 - 11.7 MeV** 9767 0.07	**2.9 - 11.7 MeV** 11544 0.01
	2.9 - 11.7 MeV 9055 0.62	**2.9 - 11.7 MeV** 9896 0.74	**2.9 - 11.7 MeV** 10855 0.51	**2.9 - 11.7 MeV** 12670 0.06
	2.9 - 11.7 MeV 9494 0.32	**2.9 - 11.7 MeV** 10135 0.39	**2.9 - 11.7 MeV** 10508 0.47	**2.9 - 11.7 MeV** 9297 0.08
Back	**9-12 cm**	**6-9 cm**	**3-6 cm**	**0-3 cm**

10 μA at 690 kPa

2.9-11.7 MeV 10936 1	**2.9 - 11.7 MeV** 9910 0.14	**2.9 - 11.7 MeV** 9190 0.14	**2.9 - 11.7 MeV** 10447 0.06	**2.9 - 11.7 MeV** 11605 0.01
	2.9 - 11.7 MeV 10159 0.46	**2.9 - 11.7 MeV** 10555 0.46	**2.9 - 11.7 MeV** 10705 0.40	**2.9 – 11.7 MeV** 10900 0.23
	2.9 - 11.7 MeV 10161 0.58	**2.9 - 11.7 MeV** 9689 0.56	**2.9 - 11.7 MeV** 10231 0.38	**2.9 – 11.7 MeV** 11455 0.03

Figure 5.4: Results of the proton energy mapping for 1 and 10 μA runs on 690 kPa of Argon. The beam enters from the right hand side. The depth into the target chamber is marked in the first set. The box on the left represents the rear foil liner. The orientation of the foil during irradiation was with its central axis along the top of the cylindrical target body and the edges of the foil met at the bottom of the target body. See Figure 4.4.

1 μA at 1551 kPa

-		**1.1 - 2.9 MeV** 7384 0.14	**2.9 – 11.7 MeV** 10204 0.19	**2.9 – 11.7 MeV** 8831 0.03
-	**1.1 - 2.9 MeV** 2030 0.03	**2.9 – 11.7 MeV** 8423 0.49	**2.9 – 11.7 MeV** 9339 0.79	**2.9 – 11.7 MeV** 10012 0.15
	0 – 1.1 MeV 1248 0.02	**2.9 – 11.7 MeV** 8654 0.49	**2.9 – 11.7 MeV** 9656 1	**2.9 – 11.7 MeV** 9999 0.26
Back	**9-12 cm**	**6-9 cm**	**3-6 cm**	**0-3 cm**

10 μA at 1551 kPa

	1.1 – 2.9 MeV 5875 0.16	**2.9 – 11.7 MeV** 9091 0.38	**2.9 – 11.7 MeV** 9335 0.26	**2.9 – 11.7 MeV** 11063 0.03
2.9–11.7 MeV 9350 0.60	**2.9 – 11.7 MeV** 8337 0.51	**2.9 – 11.7 MeV** 9432 1	**2.9 – 11.7 MeV** 10368 0.71	**2.9 – 11.7 MeV** 10937 0.08
	1.1 – 2.9 MeV 7089 0.18	**1.1 – 2.9 MeV** 6666 0.60	**2.9 – 11.7 MeV** 9595 0.66	**2.9 – 11.7 MeV** 10226 0.09

20 μA at 1551 kPa

	2.9 – 11.7 MeV 8552 0.14	**2.9 – 11.7 MeV** 9777 0.14	**2.9 – 11.7 MeV** 9566 0.07	**2.9 – 11.7 MeV** 11364 0.01
2.9–11.7 MeV 10309 0.91	**2.9 – 11.7 MeV** 9855 0.79	**2.9 – 11.7 MeV** 9817 1	**2.9 – 11.7 MeV** 10207 0.65	**2.9 – 11.7 MeV** 9696 0.08
	2.9 – 11.7 MeV 9495 0.19	**2.9 – 11.7 MeV** 10122 0.55	**2.9 – 11.7 MeV** 10696 0.50	**2.9 – 11.7 MeV** 11161 0.09

Figure 5.5: Results of the proton energy mapping for 1, 10 and 20 μA runs on 1551 kPa of Argon. The foil orientation is the same as Figure 5.4.

1 μA at 2068 kPa

- No radioactivity	**1.1 - 2.9 MeV** 4548 0.06	**2.9 - 11.7 MeV** 8404 0.91	**2.9 - 11.7 MeV** 10345 0.30	
- No radioactivity	**1.1 - 2.9 MeV** 4609 0.20	**2.9 - 11.7 MeV** 9056 1	**2.9 - 11.7 MeV** 12574 0.25	
- No radioactivity	**1.1 - 2.9 MeV** 5575 0.12	**2.9 - 11.7 MeV** 8620 0.98	**2.9 - 11.7 MeV** 10166 0.26	
Back	**9-12 cm**	**6-9 cm**	**3-6 cm**	**0-3 cm**

10 μA at 2068 kPa

0 – 1.1 MeV 1412 0.10	**1.1 – 2.9 MeV** 2472 0.01	**1.1 – 2.9 MeV** 7536 0.12	**2.9 - 11.7 MeV** 9440 0.21	**1.1 – 2.9 MeV** 3023 0.18
	1.1 – 2.9 MeV 6344 0.15	**2.9 - 11.7 MeV** 9252 0.74	**2.9 - 11.7 MeV** 10089 0.81	**2.9 – 11.7 MeV** 10476 0.13
	1.1 – 2.9 MeV 5436 0.14	**2.9 - 11.7 MeV** 8607 0.70	**2.9 - 11.7 MeV** 9594 1	**2.9 – 11.7 MeV** 11225 0.17

20 μA at 2068 kPa

2.9-11.7 MeV 8996 0.71	**2.9 – 11.7 MeV** 8045 0.12	**2.9 - 11.7 MeV** 9353 0.29	**2.9 - 11.7 MeV** 10596 0.28	**2.9 – 11.7 MeV** 11322 0.07
	2.9 – 11.7 MeV 8327 0.54	**2.9 - 11.7 MeV** 9580 1	**2.9 - 11.7 MeV** 10067 0.73	**2.9 – 11.7 MeV** 11330 0.10
	2.9 – 11.7 MeV 8005 0.33	**2.9 - 11.7 MeV** 9117 0.60	**2.9 - 11.7 MeV** 10173 0.54	**2.9 – 11.7 MeV** 11334 0.10

Figure 5.6: Results of the proton energy mapping for 1, 10, and 20 μA runs on 2068 kPa of Argon. The foil orientation is the same as Figure 5.4.

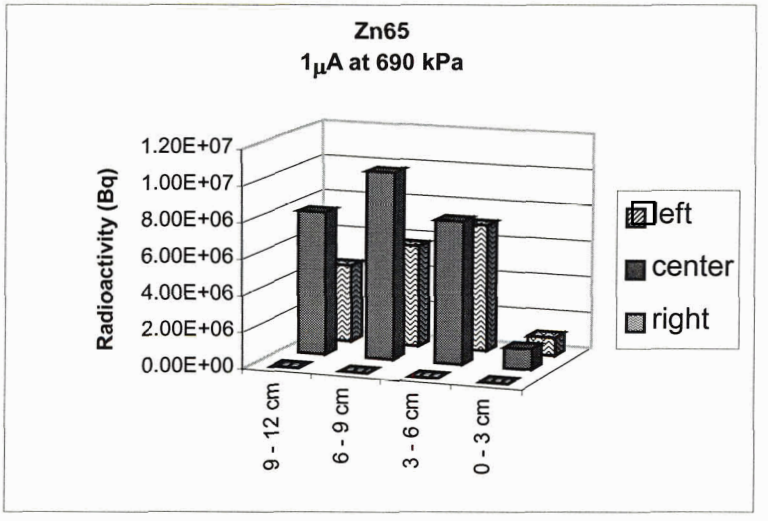

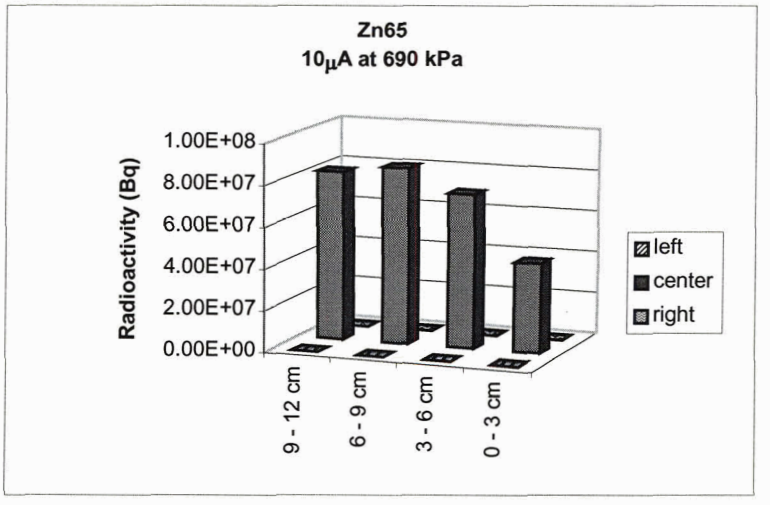

Figure 5.7: Histograms of the radioactivities of Zinc-65 produced in a foil lining for 1 and 10 μA at 690 kPa. The beam enters from the right hand side. The depth intervals corresponding to the cut foil are marked. Each column represents one cut foil segments. See Figures 4.4; 5.4-5.6. The orientation of the foil during irradiation was with its central axis along the top of the cylindrical target body and the edges of the foil met at the bottom of the target.

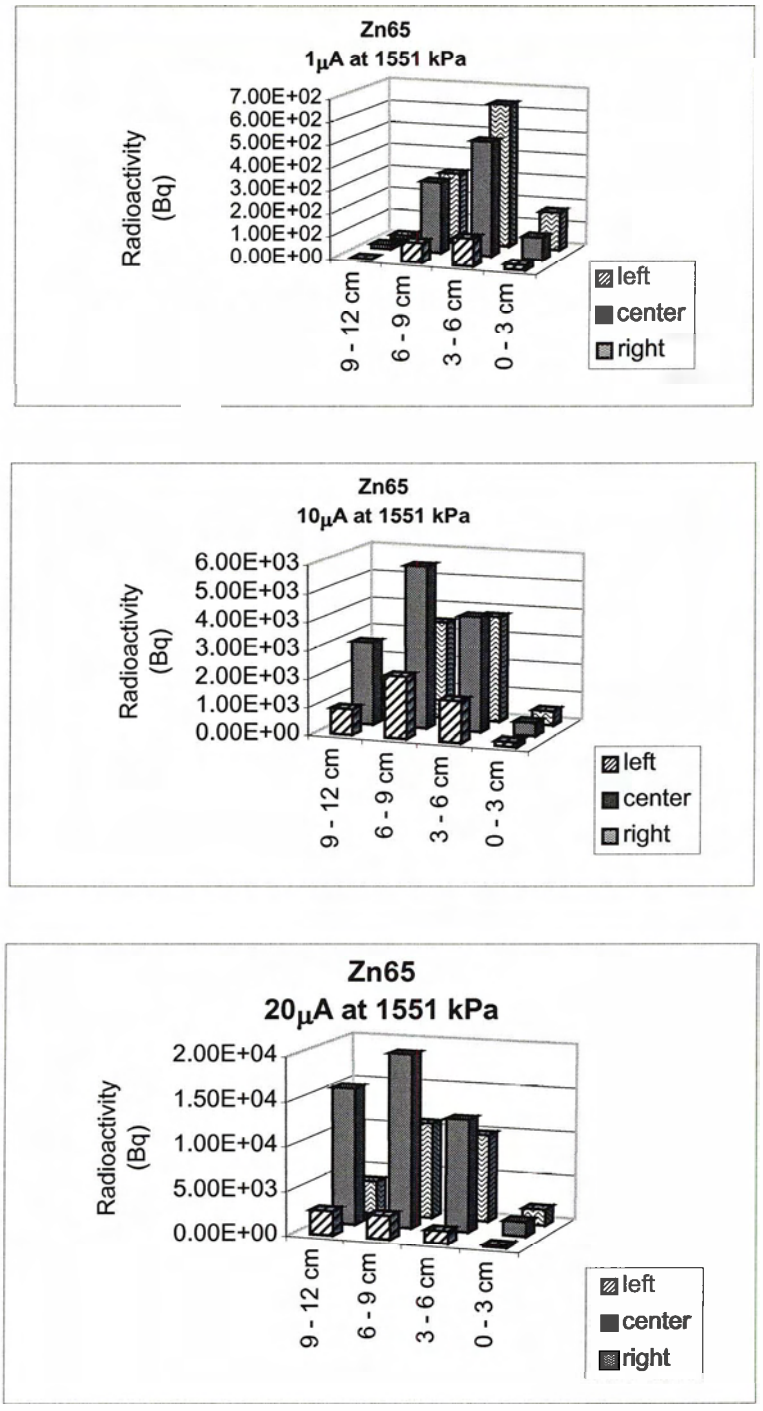

Figure 5.8: Histograms of the radioactivities of Zinc-65 produced in a foil lining for 1, 10, and 20 μA at 1551 kPa. The foil orientation is the same as Figure 5.7.

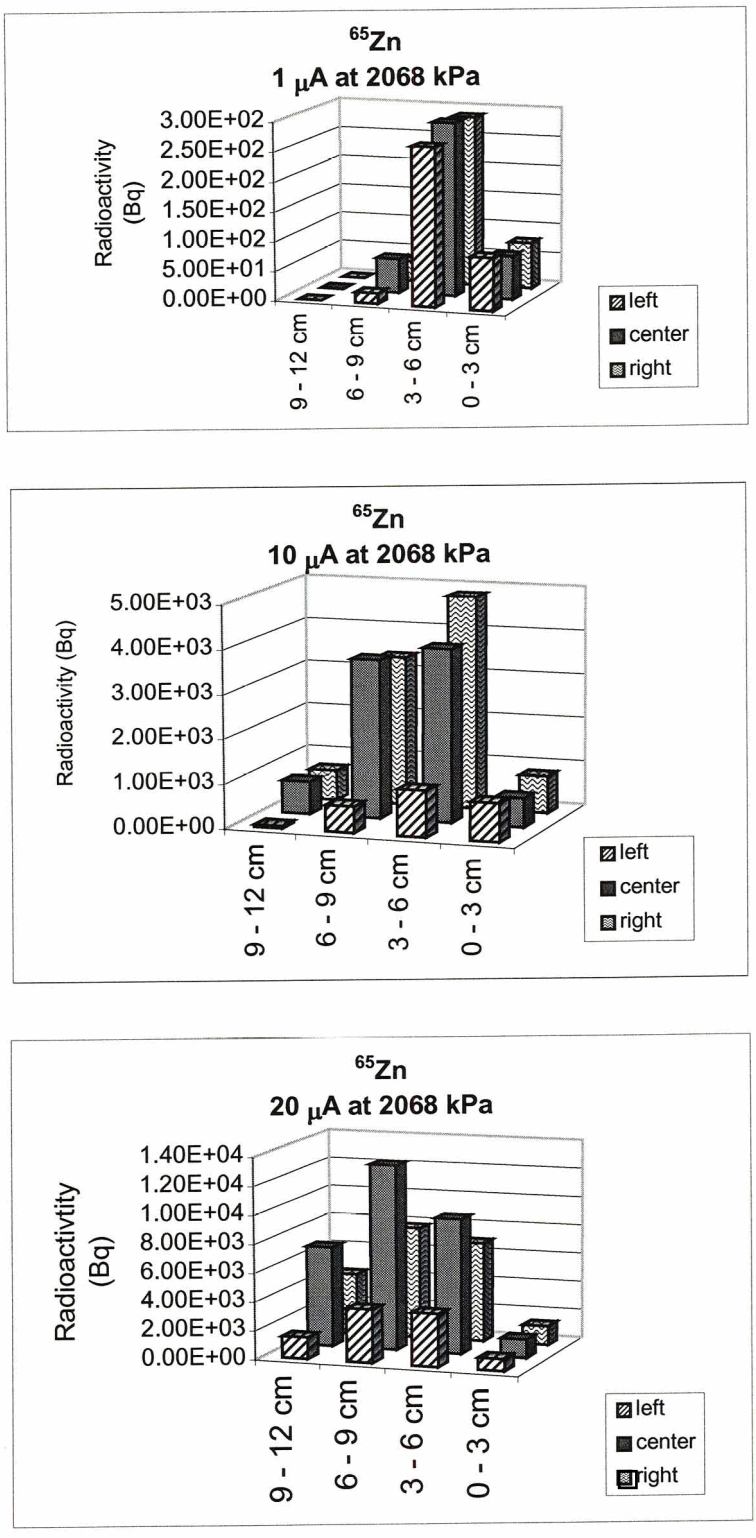

Figure 5.9: Histograms of the radioactivities of Zinc-65 produced in a foil lining for 1, 10, and 20 μA at 2068 kPa. The foil orientation is the same as Figure 5.7.

Chapter 6
Discussion and Future Prospects

In Chapter 1 we posed several questions regarding gas targets. In this section we will address these questions, in light of our results, and attempt to provide some insight into the problems surrounding gas targets.

To begin with we will address the question of whether or not the fluorescence images, seen in Figure 2.2, taken by Heselius et al [16], represent the actual beam profile. In the data sets in Figures 5.4 to 5.9 we can clearly see an increase in particle energy and induced radioactivity in the foil lining near the end of the target with increasing beam current. We also see an increase in induced radioactivity in the walls of the target, particularly along the top of the chamber. This agrees with the results found in the autoradiographic images as well as the light emission photographs taken by Heselius et al [16]. There has been some question as to whether or not the light emission photographs truly reflect the beam profile due to the fact that the image is of the photons emitted by the gas molecules during interaction with a charged particle and not an image of the ion beam itself. The results from this research project, however, support the hypothesis that the beam profile is truly reflected in those photographs.

Secondly, we have asked whether the scatter profile of an ion beam into a gas target can be predicted with the use of Monte Carlo simulations. Our results indicate that at low beam current the Monte Carlo results reflect the scatter profile reasonably well, however with increasing beam current the processes occurring within a gas target during irradiation are far more complex than what is assumed in a standard Monte Carlo program. Our results for the Monte Carlo calculations, in Table 5.1, are substantially different from those found with the foil-lined target at 10 and 20 μA, as seen in Figures 5.7 through 5.9. As an example, the Monte Carlo results would indicate that at 2068 kPa the proton beam would only reach about 9 cm depth. The results from the experimental

energy profile, however, indicate that the proton beam depth will increase with increasing beam current. At 20 μA we see full penetration through the gas.

We have also posed questions regarding the energy deposition profile along the axis of the target and if this can be used to determine the power being lost to wall interactions. We have been able to obtain approximations for the energy profile. However, the energy regime in which our targets operate largely overlaps the region of our calibration curve with poor energy resolution. Therefore we cannot make predictions as to the power deposition in the walls.

For similar reasons we cannot directly relate our results to radioisotope production yields. We can however make qualitative correlations between them. Because of the similar ranges of protons at our energies in both Argon and Nitrogen gas we will use as a comparison the production of Carbon-11 from Nitrogen gas. The proton range, according to SRIM, of 12.5 MeV protons in 1 atm of Nitrogen is 1.65 m, while 12.5 MeV protons incident on 1 atm of Argon is given as 1.56 m. Table 6.1 gives the percent yield with respect to the theoretical yield for several beam currents as given by Buckley et al [4]. The target that was used in their study had a conical chamber, not a cylindrical one as was used in this project. The data in this paper was produced on the TR13 at TRIUMF. The gas was an N_2/H_2 mix with 10% H_2. The irradiation time was 2 to 3 minutes and the gas pressure was 2068 kPa (300 psi).

Beam Current (μA)	**Yield (% theoretical)**
5	100
10	100
20	89
30	61

Table 6.1: Experimental results for the production of Carbon-11 from Nitrogen gas as determined by Buckley et al [4].

From Figure 2.3 we can see that the threshold energy for the production of Carbon-11 from Nitrogen is approximately 4 MeV. From the results for the 2068 kPa experiments, given in Figure 5.6, at 10 μA the energy of the protons reaching the back of the target is between 0 and 1.1 MeV. Therefore this is still a thick target for this reaction and is reflected in the 100% yield obtained in reference 4. This also suggests that the loss of beam due to scattering to the walls has an insignificant effect on production at this beam current. Once we increase the beam current to 20 μA, however, the energy of the protons reaching the back is between 2.9 and 11.7 MeV. Therefore, we may no longer have a thick target, which explains why the yield is lower than theoretically expected. This observation is even more dramatic once the beam current is increased to 30 μA, at which point the yield drops to only 61 % of the theoretical yield.

As mentioned in Section 1.2 both an increase in particle penetration due to density reduction and loss of protons due to scattering into the target chamber walls has been noted as possible sources of reduced radioisotope production yields. In order to compare the amount of protons lost to the walls of the target through scatter to those lost to the back of the target by increased penetration from density reduction we have summed the Zinc-65 activities produced in each foil section to obtain the radioactivity in the entire copper foil lining and from this calculated the percent total activity (i.e.- percentage of lost beam) in the back liner foil and wall liner foil. This total activity is related to the amount of beam lost. The percentages for the 690 kPa, 1551 kPa and 2068 kPa experiments can be found in Table 6.2. For the 1 μA runs for both 1551 kPa and 2068 kPa 100% of the activity produced was in the walls. From this we can see that the most significant amount of beam lost is to the outer walls of the target. However, this is simply the percentages of lost beam and cannot be correlated to the amount of total beam without knowing the total number of protons incident on the target. It is also difficult to relate this to production yields without knowing the energy of the scattered protons. Since the threshold for producing Zinc-65 is around 2.5 MeV many of these protons may be below the 4 MeV threshold for Carbon-11 production. For example, the study

preformed by Buckley et al [4] reported 100% yield at 10μA, therefore the beam being lost to scatter to the walls is insignificant in either the number of protons which are scattered or the energy of the scattered protons to affect the total yield.

Pressure (kPa)	Beam Current (μA)	Foil Position	Percent Total Activity (%)
690	1	Walls	79
		Back	21
	10	Walls	78
		Back	22
1551	10	Walls	89
		Back	11
	20	Walls	82
		Back	18
2068	10	Walls	98
		Back	2
	20	Walls	87
		Back	13

Table 6.2: Percentages of total Zinc-65 activity produced in Copper foils lining the inner target chamber.

The total Zinc-65 radioactivity for the lining of the walls and back has been used to compare the increase in beam lost to wall interactions with increased beam current. The total activity for each experiment has been divided by the respective beam current to obtain the amount of radioactivity produced per μA. This was then divided by the radioactivity produced at 1 μA in order to observe the number of times increase. The numbers can be seen in Table 6.3. Ideally, we would like to optimize our target chamber to allow for irradiation of the gas with as high a beam current as possible. Increased beam currents, however, result in increased penetration and scatter to the walls, particularly to the top of the target chamber. With our comparison to the results found in reference 4, by Buckley et al, the scatter to the walls does not appear to be a significant contributor at these beam currents, however, we cannot tell what contribution it will

make at much higher beam currents. One possible solution to minimize this loss from scatter may be a target chamber with a water-drop cross-sectional shape. This would accommodate for the larger amount of radioactivity produced in the foil lining at the upper portion of the chamber as seen in figures 5.7 through 5.9.

Pressure (kPa)	Beam Current (μA)	Number of times increase over a 1 μA run
690	1	1
	10	6.3
1551	1	1
	10	1.3
	20	2.2
2068	1	1
	10	1.8
	20	2.9

Table 6.3: The factor by which the radioactivity produced in a foil lining increases per μA.

Future experiments would include varying the target radius, pressure and target gas. As well as including different particle energies and beam current regimes. The use of a different foil lining material, which could provide more sensitivity in the 3 to 11 MeV range, would also be beneficial. In addition to this approach we would like to consider the question of why and how different radioactive species are trapped in the target body walls. Could there be a relation between particle scatter and/or energy with the radionuclide "sticking" process? The "sticking" of the produced radioactive species during irradiation to the target body walls has been noted as another contributing factor to the decrease in recoverable product yield [4, 5].

The development of a Monte Carlo program, which would include the effects of thermal convection and heat transfer on the proton path and energy within a gas target, would be beneficial to tracking the reaction cross-sections and hence optimizing production capabilities.

Chapter 7
Conclusions

With both autoradiography and the foil lined target experiments we were able to demonstrate the increase of pressure and particle penetration within a gas target with increasing beam current. This is consistent with the work done by Heselius et al [16] who have taken fluorescence images of the light emitted by a gas target during bombarded with a beam of charged particles. This indicates that these images do indeed correctly resemble the beam path into a gas target.

The Monte Carlo model for proton scattering modeled the low beam current experiments reasonably well, however, as beam current increased this model was no longer valid in determining the beam profile in the target. Monte Carlo models for particle penetration generally do not include corrections for density variations, which is a result of heat being deposited in the target from the incident particles.

We have been able to provide some axial energy profile information from our foil lined target experiments. However, because the energy window lies within a large flat region on the calibration curve, a precise determination of this energy profile was not possible.

References

[1] T.J. Ruth, "Nuclear Medicine", Encyclopaedia of Applied Physics, Vol. 11, VCH Publishers, Inc., 1994

[2] E.J. Hoffman, M.E. Phelps, "Positron Emission Tomography: Principles and Quantitation" in "Positron Emission Tomography and Autoradiography: Principles and Applications for the Brain and Heart", Phelps, M., J. Mazziotta and H. Schelbert. Eds. Raven Press, New York. 1986 p237-286.

[3] G. T. Bida, T.J. Ruth, and A.P. Wolf, "Experimentally determined thick target yields for the $^{14}N(p,\alpha)^{11}C$ reaction", Radiochimica Acta, 27(1980)181.

[4] K.R. Buckley, J. Huser, S. Jivan, K.S. Chun, T.J. Ruth, "^{11}C-methane production in small volume, high pressure gas targets", Radiochimica Acta, 88(2000)201.

[5] K.R. Buckley, S. Jivan, T.J. Ruth, "Improved yields for the in situ production of $[^{11}C]CH_4$ using a niobium target chamber", Nuclear Medicine and Biology 31(2004)825.

[6] M.L. Firouzbakht, D.J. Schlyer, A.P. Wolf, "Effect of foil material on the apparent yield of the $^{124}Xe(p, x)^{123}I$ reaction", International Journal of Radiation Applications and Instrumentation, 43(1992)741.

[7] N.V. Kurenkov, V.P. Lunev, V.S. Masterov, Y.N. Shubin, "Excitation functions for the formation of the neutron deficient nuclei Iodine-123, Xenon-123 and Caesium-123. Calculated and experimental data", Applied Radiation and Isotopes, 44(1993)883.

[8] D.R. Christman, R.D. Finn, K.I. Karlstrom, A.P. Wolf, "The production of ultra high activity ^{11}C-labeled hydrogen cyanide, carbon dioxide, carbon monoxide and methane via the $^{14}N(p,\alpha)^{11}C$ reaction (XV)", International Journal of Applied Radiation and Isotopes, 26(1975)435.

[9] M.C. Lagunas-Solar, O.F. Carvacho, "Cyclotron Production of PET Radionuclides: No-carrier-added Fluorine-18 with High-energy protons on Natural Neon Gas Targets", Applied Radiation and Isotopes 46(1995)833.

[10] T.J. Ruth, A.P. Wolf, "Absolute Cross Sections for the Production of ^{18}F via the $^{18}O(p,n)^{18}F$ Reaction", Radiochimica Acta, 26(1979)21.

[11] T. E. Barnhart, A. K. Converse, K. A. Dabbs, R. J. Nickles, K. Buckley, S. Jivan, T. J. Ruth and A. D. Roberts. "Water-cooled grid support for high-power irradiation with thin target windows", Applied Radiation and Isotopes, 58(2003)21.

[12] Z. Kovacs, F. Tarkanyi, S.M. Quaim, G. Stocklin, "Production of 6.5 h ^{82m}Rb via the ^{82}Kr(p, n)- process at a low-energy cyclotron- a potential substitute for ^{82}Rb", International Journal of Radiation Applications and Instrumentation [A], 42(1991)831.

[13] J. Gorres, K.U. Kettner, H. Krawinkel and C. Rolfs, "The influence of intense Ion beams on gas target densities", Nuclear Instruments and Methods, 177(1980)295.

[14] L.P. Robertson, B.L. White, K.L. Erdman, "Beam Heating effects in Gas Targets", Review of Scientific Instruments, 32(1961)1405.

[15] S. Lapi, T.J. Ruth, A. Zyuzin, J.M. D'Auria, "Development of an intense O-15 radioactive ion beam using low energy protons", Nuclear Instruments and Methods In Physics Research B, 204(2003)444.

[16] S.-J. Heselius, P. Lindblom, O. Solin, "Optical studies of the influence of an intense ion beam on high-pressure gas targets", International Journal of Applied Radiation and Isotopes, 33(1982)653.

[17] R.D. Evans, "The Atomic Nucleus", McGraw Hill Book Company, Inc., Toronto, 1955.

[18] Physics Letters B, "Review of particle physics", Volume 592, Issues 1-4, pp.242 243, Elsevier, San Diego, 2004.

[19] S.P. Ahlen, "Theoretical and experimental aspects of the energy loss of relativistic heavilyionizing particles", Reviews of Modern Physics, 52(1980)121.

[20] K.S. Krane, "Introductory Nuclear Physics", John Wiley and Sons, Inc., Toronto, 1988.

[21] J.F. Ziegler, "The Stopping of Energetic Light Ions in Elemental Matter", Journal of Applied Physics/Reviews of Applied Physics, 85(1999)1249.

[22] Online SRIM documentation: http://www.srim.org/SRIM/SRIMINTRO.htm Last accessed 11/04.

[23] SRIM documentation on Shell Corrections:
http://www.srim.org/SRIM/SRIMPICS/IONIZ.htm
Last accessed 10/04.

[24] W.D. Ehmann, "Radiochemistry and Nuclear Methods of Analysis", John Wiley & Sons, Inc., Toronto, 1991.

[25] D.J. Schlyer, P.S. Plascjak, "Small angle multiple scattering of charged particles in cyclotron target foils- a comparison of experiment with simple theory", Nuclear Instruments And Methods In Physics Research B56/57(1991)464.

[26] H.-J. Helmeke, H. Hundeshagen, "Design of gas targets for the production of medically used radionuclides with the help of Monte-Carlo simulation of small angle multiple scattering of charged particles", Applied Radiation and Isotopes, 46(1995)751.

[27] H.A. Bethe, "Molière's theory of Multiple Scattering", Physics Review, 89(1953)1256.

[28] J.B. Marion, B.A. Zimmerman, "Multiple scattering of charged particles", Nuclear Instruments and Methods, 51(1967)93.

[29] J.F. Ziegler, J.P. Biersack, U. Littmark, "The stopping and range of ions in solids", Volume 1, Pergamon Press, Toronto, 1985.

[30] J.P. Biersack, L.G. Haggmark, "A Monte Carlo computer program for the transport of energetic ions in amorphous targets", Nuclear Instruments and methods, 174(1980)257.

[31] D.K. McDaniels, I. Bergqvist, D. Drake and J.T. Martin, "Beam heating in gas targets", Nuclear Instruments and Methods, 99(1972)77.

[32] M. Oselka, J.E. Gindler and A.M. Friedman, "Non-linear Behaviour of Gas Targets for Isotope Production", International Journal of Applied Radiation and Isotopes, 28(1977)804.

[33] B.W. Wieland, D.J. Schlyer, T.J. Ruth and A.P. Wolf, "Deuteron Beam Penetration in a Neon Gas Target for Producing Fluorine-18", Journal of Labelled Compounds and Radiopharmaceuticals, 18(1981)27.

[34] T. Vandewalle and C. Vandecasteele, "Optimisation of the Production of $^{11}CO_2$ by Proton Irradiation of Nitrogen Gas", International Journal of Applied Radiation and Isotopes, 34(1983)1459.

[35] T.J. Ruth and A.P. Wolf, ""Small" Accelerator, Radionuclide and Radiopharmaceutical Production", IEEE Transactions in Nuclear Science, NS-26 (1979) 1710.

[36] B.W. Wieland, D.J. Schlyer and A.P. Wolf, "Charged Particle Penetration in Gas Targets Designed for Accelerator Production of Radionuclides Used in Nuclear Medicine", International Journal of Applied Radiation and Isotopes, 35(1984)387.

[37] V. Casella, T. Ido. A.P. Wolf, J.S. Fowler, R.R. MacGregor and T.J. Ruth, "Anhydrous F-18 Labeled Elemental Fluorine for Radiopharmaceutical Preparation", Journal of Nuclear Medicine, 21(1980)750.

[38] S-J. Heselius, P. Lindblom and O. Solin, "Interferometric Studies of the Influence of an Intense Ion Beam on High Pressure Gas Targets", Journal of Labelled Compounds and Radiopharmaceuticals, 19(1982)1343.

[39] O. Solin, S-J. Heselius, P. Lindblom and E.M. Nyman, "Density Reduction and Temperature Mapping in a Ne-Gas Target", Journal of Labelled Compounds and Radiopharmaceuticals, 21(1984)1279.

[40] S-J. Heselius, P. Malmborg, O. Solin and B. Langstrom, "Production of Carbon-11 with Respect to Specific Radioactivity- A Target Study", Journal of Labelled Compounds and Radiopharmaceuticals, 21(1984)475.

[41] S-J. Heselius and O. Solin, "A Model for Beam Penetration in Gas Targets", Journal of Labelled Compounds and Radiopharmaceuticals, 23(1986)1389.

[42] J.J.L. Mulders, "Yield Curves and Beam Current Dependent Production Rates of Rb Radioisotopes Produced by Protons on a Krypton Gas Target", International Journal of Applied Radiation and Isotopes, 35(1984)475.

[43] K. Buckley, S. Lapi, J. Publicover, T.J. Ruth, and S. Jivan, "Design Considerations for High Power Gas Targets: Part II", Division of Nuclear Chemistry and Technology, 226th ACS National Meeting, New York, NY, September 7-11, 2003.

[44] P.W. Wojciechowski, M. Sajjad, R.M. Lambrecht, "A semi-quantitative approach to the design, analysis and operation of a gas target system", Applied Radiation and Isotopes, 39(1988)429.

[45] K. Krane, "Modern Physics", 2nd Ed., John Wiley & Sons, Inc., Toronto, 1996.

[46] The International Atomic Energy Agency website for nuclear data services: http://www-nds.iaea.or.at/medical/n4p11c0.html
Last accessed on 11/04.

[47] The National Nuclear Data Center (nndc) at Brookhaven National Laboratories: http://www.nndc.bnl.gov
Last accessed on 11/04.

[48] Online PerkinElmer documentation:
http://las.perkinelmer.com/content/ApplicationNotes//
notesFROMcurrentSite/CYC004.pdf
Last accessed on 10/04.

[49] The International Atomic Energy Agency website for nuclear data services: http://www-nds.iaea.or.at/medical/monitor_reactions.html
Last accessed on 11/04.

[50] Knoll, G.F., "Radiation Detection and Measurement", John Wiley & Sons, Inc., Toronto, 1979.

Appendix A
High Purity Germanium Detectors (HPGe)

Also known as intrinsic germanium detectors, these semiconductor detectors are largely replacing their lithium-drifted counterparts due to their ability to be stored at room temperature [24, 50].

The most appealing characteristic of germanium detectors is their excellent energy resolution. This lends itself well to applications involving gamma ray spectrometry of complex energy spectra because it allows for discrimination of closely spaced photopeaks.

A block diagram of the detector system used for this project can be found in figure B.1. The system consists of an Ortec coaxial HPGe detector with a built-in preamplifier in an upright position and is surrounded by in-house custom made shielding. The electronics used consist of an Ortec amplifier, model 572, an Ortec high voltage power supply, model 459, both set in a B.L. Packer Co. (blp) nuclear instrumentation modules (NIM) bin, model NB-10. The multi-channel analyzer (MCA) is a Nucleus™ personal computer analyzer (PCA-II) computer plug-in board and the data is collected and displayed using Nucleus Inc. PCA-II software.

Prior to use, an energy calibration was performed and an absolute efficiency versus energy curve was constructed. Both were executed using a multi-line calibrated point source consisting of both ^{125}Sb ($t_{1/2}$= 2.76y), and ^{154}Eu ($t_{1/2}$= 8.59y). This source has many peaks over our range of interest, from approximately 100 keV to 1500 keV. The Nucleus software has a built-in energy calibration option, which allows the user to assign energies to several channels and it then interpolates the energies in between.

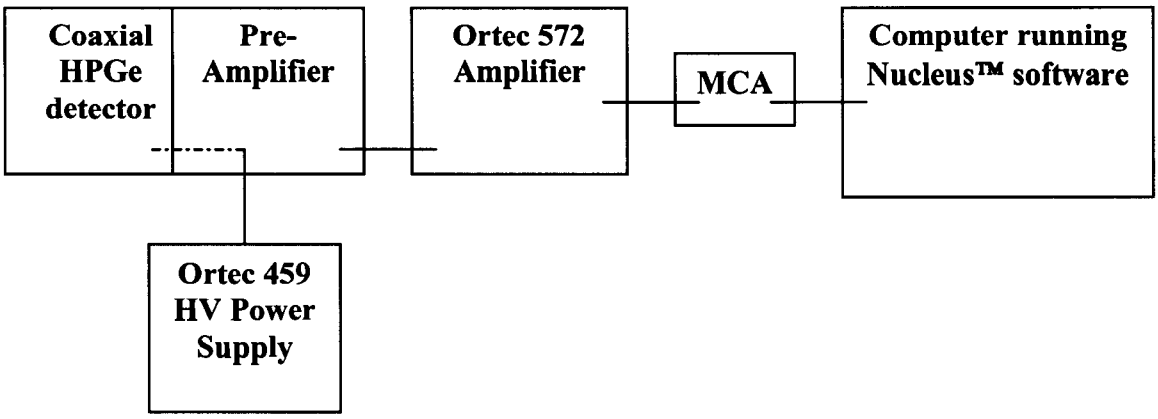

Figure A.1: Block diagram of HPGe detector system setup.

The absolute efficiency was calculated using the following equation [50];

$$\varepsilon_{abs} = \frac{\text{Number of pulses recorded}}{\text{Number of quanta emitted by the source}}$$

Where

ε_{abs} is the absolute efficiency.

The number of pulses recorded is the number of counts stored for each peak by the Nucleus software

and *the number of quanta emitted by the source* is the radioactivity, in Bequerels (1Bq= 1disintegration per second), multiplied by the count time in seconds.

The source was calibrated on September 01, 1988 and the radioactivity at this time was made available through personal communication with Dr. A. Zyuzin. To obtain the number of quanta emitted by the source, the present radioactivity of each isotope must be calculated to account for decay. The following equation was used:

$$A=A_0e^{-\lambda t}$$

Where:

A is the present radioactivity of the isotope

A_0 is the calibrated activity as of 09/01/88

λ is the decay constant and is equal to $\ln 2 / t_{1/2}$

and t is the decay time

The absolute efficiencies were calculated for three different detector-source distances; one each at 4 cm, 17.5 cm and 60 cm from the detector surface. These geometries were chosen to maximize the number of counts observed by the detector without obtaining too much dead time or coincidence summing. The $\log(\varepsilon_{abs})$ versus log(Energy) curve for the 4cm distance geometry can be found in Figure A.2.

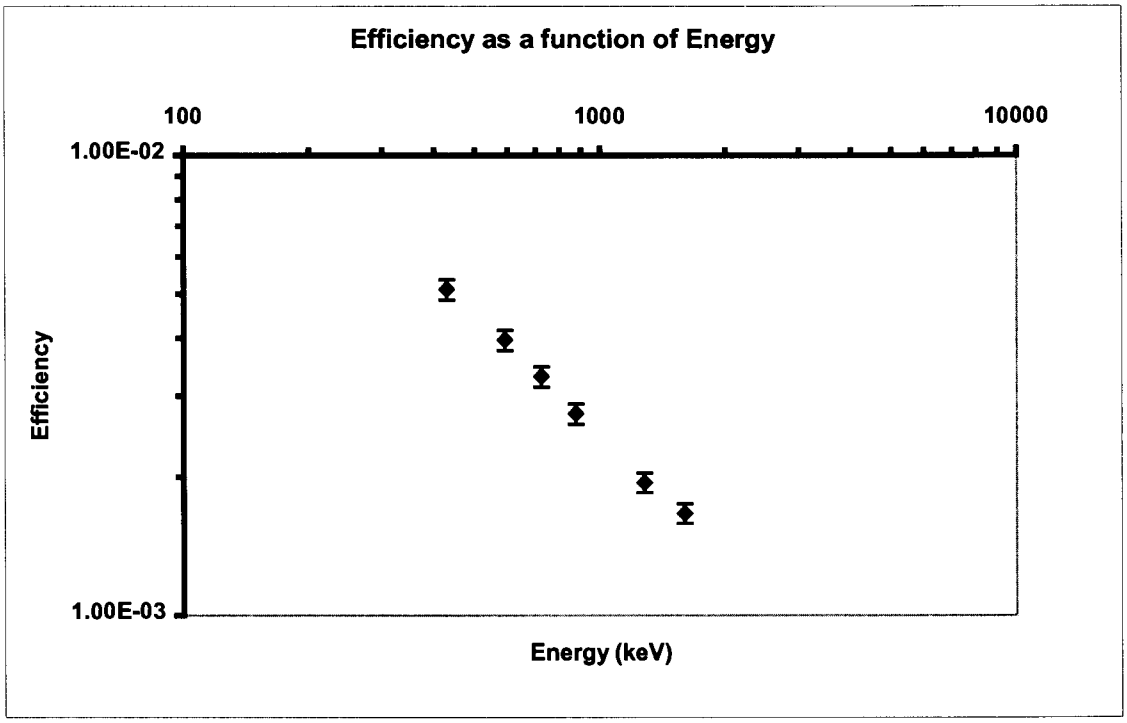

Figure A.2: Absolute efficiency versus Energy (keV) log-log curve for a geometry of 4 cm distance from the detector surface.

Appendix B
Data

The results for the ratio calculations from the foil lined target experiments are given below in Tables B.1, B.2 and B.3. The foil number represents the location of the cut foil piece with respect to the foil liner. See Figure B.1 for the location and number. Foil number "B" is the foil lining the back of the target. The proton beam enters from the right hand side, while the top and bottom edges meet at the bottom of the target chamber to form a cylindrical liner. It should be noted that the top edge of the foil overlapped the bottom slightly when lining the target.

10	**7**	**4**	**1**
11	**8**	**5**	**2**
12	**9**	**6**	**3**

Figure B.1- The foil number location for the cut foil liner is given. The proton beam enters from the right hand side. Foil number B is associated with the foil lining the back of the target.

Beam Current (μA ± 0.5 μA)	Foil Number	Ratio	Zinc-65 Radioactivity (Bq)
1	1	11544 ± 1748	12.8
	2	12670 ± 756	89.1
	3	9297 ± 538	106.5
	4	9767 ± 595	97.5
	5	10855 ± 525	725.5
	6	10508 ± 555	669.9
	7	9845 ± 392	292.9
	8	9896 ± 259	1045.8
	9	10135 ± 329	555.7
	10	9344 ± 389	321.4
	11	9055 ± 268	874.2
	12	9494 ± 364	451.4
	B	10283 ± 269	1417.1
10	1	11605 ± 505	185.9
	2	10900 ± 512	3942.6
	3	11455 ± 492	578.2
	4	10447 ± 389	1016.8
	5	10705 ± 469	6930.0
	6	10231 ± 505	6671.1
	7	9190 ± 780	2504.4
	8	10555 ± 520	8059.8
	9	9689 ± 219	9855.9
	10	9910 ± 349	2407.2
	11	10159 ± 252	8014.9
	12	10161 ± 244	10210.0
	B	10936 ± 238	17466.5

Table B.1: Results of the 690 kPa experiments.

Beam Current (μA ± 0.5 μA)	Foil Number	Ratio	Zinc-65 Radioactivity (Bq)
1	1	8831 ± 1015	22.0
	2	10012 ± 566	98.1
	3	9999 ± 452	166.5
	4	10204 ± 535	121.5
	5	9339 ± 284	503.7
	6	9656 ± 276	634.5
	7	7384 ± 499	86.6
	8	8423 ± 326	310.7
	9	8645 ± 339	310.3
	10	-	0.0
	11	2030 ± 274	18.7
	12	1248 ± 206	15.7
	B	-	0.0
10	1	11063 ± 592	160.9
	2	10937 ± 385	470.0
	3	10226 ± 362	506.7
	4	9335 ± 241	1474.2
	5	10368 ± 408	4095.1
	6	9595 ± 420	3783.5
	7	9091 ± 246	2200.9
	8	9432 ± 207	5770.8
	9	6666 ± 169	3464.3
	10	5875 ± 257	922.5
	11	8337 ± 242	2941.4
	12	7089 ± 332	1055.5
	B	9350 ± 338	3484.7
20	1	11364 ± 561	206.3
	2	9696 ± 406	1662.3
	3	11161 ± 449	1814.1
	4	9566 ± 477	1406.4
	5	10207 ± 241	12718.2
	6	10696 ± 275	9851.4
	7	9777 ± 426	2686.0
	8	9817 ± 230	19652.9
	9	10122 ± 287	10801.5
	10	8552 ± 455	2775.6
	11	9855 ± 270	15486.9
	12	9495 ± 239	3741.2
	B	10309 ± 289	17942.8

Table B.2: Results of the 1551 kPa experiments.

Beam Current (μA ± 0.5 μA)	Foil Number	Ratio	Zinc-65 Radioactivity (Bq)
1	1	10345 ± 727	88.8
	2	12574 ± 925	73.5
	3	10166 ± 788	77.3
	4	8404 ± 403	266.4
	5	9056 ± 421	292.0
	6	8620 ± 420	287.5
	7	4548 ± 627	17.8
	8	4609 ± 367	57.4
	9	5575 ± 562	34.2
	10	-	0.0
	11	-	0.0
	12	-	0.0
	B	-	0.0
10	1	3023 ± 124	852.5
	2	10476 ± 355	647.1
	3	11225 ± 352	827.4
	4	9440 ± 294	1034.5
	5	10089 ± 433	3902.9
	6	9594 ± 405	4827.9
	7	7536 ± 351	581.7
	8	9252 ± 224	3579.7
	9	8607 ± 219	3369.9
	10	2472 ± 302	48.2
	11	6344 ± 191	726.0
	12	5436 ± 177	677.0
	B	1412 ± 80.5	483.6
20	1	11322 ± 628	833.5
	2	11330 ± 548	1272.2
	3	11334 ± 567	1322.4
	4	10596 ± 375	3646.1
	5	10067 ± 273	9391.93
	6	10173 ± 316	6924.5
	7	9353 ± 394	3681.2
	8	9580 ± 267	12907.0
	9	9117 ± 318	7766.0
	10	8045 ± 679	1492.6
	11	8327 ± 364	6946.8
	12	8005 ± 467	4233.1
	B	8996 ± 377	9104.5

Table B.3: Results of the 2068 kPa experiments.